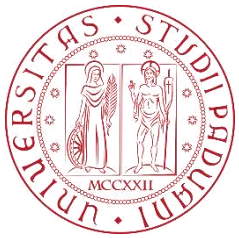

UNIVERSITÀ DEGLI STUDI DI PADOVA

Dipartimento di Fisica e Astronomia “Galileo Galilei”

Corso di Laurea in Fisica

Tesi di Laurea

Osservazioni potenziali di sistemi binari di nane bianche mediante il rivelatore di onde gravitazionali LGWA

Observing double-white dwarfs with the Lunar GW Antenna

Relatore

Prof. Jean Pierre Zendri

Correlatore

Prof. Jan Harms

Laureando

Giovanni Benetti

Anno Accademico 2023/2024

Observing double-white dwarfs with the Lunar GW Antenna

Giovanni Benetti

15 July 2024

ABSTRACT

The Lunar GW Antenna (LGWA) is a proposed GW detector with an observation band spanning from about 1mHz to 1Hz. The LGWA would be able to detect signals from double white dwarfs (DWDs) outside our galaxy. This opens the possibility for breakthroughs in our understanding of SN Ia progenitors and improved calibration of SN Ia for measurements of the Hubble constant. Important would be to identify the host galaxies of the detected DWDs. In this work, I will study the capabilities of LGWA to detect and localize DWDs in terms of its sky locations and distances. The analysis will be carried out with realistic distributions of the masses of the DWDs obtained from current galactic population models.

SOMMARIO

Il Lunar Gravitational Wave Antenna (LGWA) è una proposta per un rivelatore di onde gravitazionali che esplorerà la banda di frequenza dal mHz a 1 Hz. LGWA sarà in grado di rivelare segnali dalle binarie di nane bianche (DWD), all'interno e all'esterno della nostra galassia. Ciò apre la possibilità a fondamentali avanzamenti nella conoscenza dei progenitori delle SN Ia, ed a nuovi metodi di calibrazione delle distanze delle SN Ia, usate per determinare la costante di Hubble. Sarà quindi importante identificare le galassie ospiti delle DWD rilevate. In questa tesi, studierò le prestazioni di LGWA in relazione alla rivelazione e localizzazione delle DWD, in particolare per quanto riguarda le distanze e la posizione in cielo delle sorgenti. L'analisi sarà effettuata usando distribuzioni realistiche dei parametri delle DWD, ottenute usando gli attuali modelli di formazione ed evoluzione stellare e di struttura delle galassie.

Key words: Gravitational Waves – Astrophysics – Detectors

1 LIST OF ABBREVIATIONS

CE	Common Envelope
CMB	Cosmic Microwave Background
DD	Double Degenerate
DWD	Double White Dwarfs system
FAR	False Alarm Rate
HST	Hubble Space Telescope
IMF	Initial Mass Function
JWST	James Webb Space Telescope
LISA	Laser Interferometer Space Antenna
LIGS	Lunar Inertial Gravitational-wave Sensor
LGWA	Lunar Gravitational Wave Antenna
MW	Milky Way
PE	Parameter Estimation
PSD	Power Spectral Density
SD	Single Degenerate
SFH	Star Formation History
SFR	Star Formation Rate
SN	Supernova
SNR	Signal to Noise Ratio
WD	White Dwarf

2 DWDS: STRUCTURE AND CHARACTERISTICS

The subject of study of this thesis are Double White Dwarfs systems (DWD) as seen from the Lunar Gravitational Wave Antenna (LGWA). In this section I present a description of these objects, with an approach finalized to the following characterization of the LGWA response to the present DWD population.

2.1 Late stages of stellar evolution

In stable main-sequence stars, the ionized gas would tend to collapse towards the center under the gravitational force; the pressure developed at the core allows for nuclear fusion reactions to start, leading to a counter-pressure that expands the system. The star eventually reaches the stable equilibrium between these two forces, and burns the hydrogen at the core producing almost exclusively ^{4}He nuclei. After a certain time span, which heavily depends on the initial mass of the star, the remaining hydrogen is not enough to sustain anymore the energy production needed for the equilibrium to be maintained. The gravitational force overcomes and the star enters the late stages of the stellar evolution: the final result, after the transition phases, can be either a light remnant (brown dwarf) with $M < 0.08 M_\odot$, or

a compact remnant for superior masses. In this case, the major part of the star's hydrogen envelope is ejected (fig. 1) leaving behind the non-hydrogen core; for initial masses $M_i < 8M_\odot$ the collapse of this remnant can be stopped by the electron degeneracy pressure as the mean distance between the electrons becomes comparable with their thermal wavelength

$$\lambda = \frac{h}{\sqrt{2\pi m_e k_B T}}$$

where m_e is the electron mass, k_B the Boltzmann constant and T the kinetic temperature of the electron gas. Coulomb corrections are neglected for now. At this point, the degenerate Fermi gas of electrons provides a degeneracy pressure that stabilizes the star. The properties of the star can be found by imposing the equilibrium between the gravitational force and the degeneracy pressure; In the idealized case of non-relativistic, charge-less fermions a good approximation of the radius-mass relation is given by (Padmanabhan 2001):

$$R(M) \approx \frac{0.022}{\mu_e}\left(\frac{M}{M_{Ch}}\right)^{-1/3}\left[1-\left(\frac{M}{M_{Ch}}\right)^{4/3}\right]^{1/2} R_\odot \qquad (1)$$

with $M_{Ch} \simeq 1.4M_\odot$, $\mu_e = \frac{\rho}{n_e m_p}$, with n_e number density of the electrons, namely the number of nucleons per electron; μ_e is used as an alias parameter to replace the specific volume of the degenerate Fermi gas $v = V/N$ with $\mu_e n_p \rho^{-1}$, making explicit the density ρ, that is a key parameter for gravitational considerations. μ_e is left as a parameter to account for the different isotopic compositions that can be found, but in any case $\mu_e \approx 2$. Note that this equation diverges for $M \to 0$ and becomes 0 at $M = M_{Ch}$. Both these limits are not physical, as for the former the electron gas would not be degenerate for $R > R_\odot$ at least (in addition, Coulomb corrections are not negligible at low densities), and for $M \approx M_{Ch}$ the neutronisation process begins, leading to other remnants. The radius decreases as the mass increases: the bigger is the mass, the smaller is the compact object. The resulting WD eventually consists in a non-degenerate gas of ions (the nuclei produced by the fusion reactions) and a degenerate gas of electrons. The ion gas composition depends on the WD mass, and can be approximately subdivided in three categories:

- For $M \lesssim 0.5M_\odot$, the conditions are not sufficient for He to start fusion in the transition phases; the result is a He WD
- For $0.5M_\odot \lesssim M \lesssim 1.2M_\odot$, the He starts burning, and the main products are C and O; the result is a CO WD
- For $1.2M_\odot \lesssim M \lesssim M_{Ch}$, the C burns producing Ne; the result is a NeO WD.

With higher masses, the neutronisation process begins, and the final result is a neutron star with $M \approx 1.4M_\odot$ supported by the degeneracy pressure of the neutrons, arranged in a Fermi gas; at higher masses ($M_{\text{remnant}} > 3M_\odot$) the system collapses forming a black hole, since the degeneracy pressure of the neutron gas cannot balance the gravitational pressure, similarly to what happens for the electronic Fermi gas in a WD when the Chandrasekhar mass is surpassed.

2.2 Double White Dwarfs and SN Ia

Our galaxy's initial stellar population is characterized by a starting binary fraction of $\approx 50\%$; this means that after the late evolutionary stages of both the stars, if the initial masses belonged to the interval $0.95M_\odot \lesssim M_i \lesssim 10M_\odot$, the remnant will likely be a DWD system. The processes that lead to the formation of a short-period DWD that will merge in less than a Hubble time are complex and involve at least two episodes of mass transfer, one of which is a Common Envelope (CE) phase. During this brief period, both the stars are embedded in a bigger gas envelope resulting from the expansion of one of the two stars in the latter stage of evolution. The envelope exerts a drag force on the system, that consequently shrinks; the energy lost by drag contributes to heating the CE, which is eventually expelled, leaving a short period DWD binary system. The resulting binary than slowly shrinks by emission of gravitational waves and finally merges; the merging event between two CO WDs with $M_{tot} \gtrsim M_{Ch}$ is a possible candidate for SN Ia events (Webbink (1984), Wang & Han (2012)). A SN Ia is a thermonuclear explosion believed to be generated by the accretion of a CO WD from a companion above the Chandrasekhar mass (in the following the nature of this companion is precised). The result is a collapse due to the insufficient electron degeneracy pressure, starting a carbon-burning phase that produces heavier elements up to iron. This sudden energy production results in an explosion that incinerates the star, probably leaving no further remnants. The energy emission is so strong that the SN can become brighter than the whole host galaxy, thus visible from very large distances (fig. 2). It remains visible for approximately 100-200 days or more depending on the specific object, describing a characteristic light curve.

Figure 1. Planetary nebula NGC 6853, a remnant of the ejection of the outer shell in the late evolution of the star; it is visible the WD remnant at the center. Image taken with the Asiago Schmidt 67/92 telescope, INAF.

SN Ia have a central role in astrophysics: above all, SN Ia luminosities are used to deduce a measure of cosmological redshift (Phillips (1993), Riess et al. (1995), and for a recent measurement with James Webb Space Telescope (JWST) Pascale et al. (2024)), exploiting the luminosity curves as standard candles. The value of the Hubble constant obtained from this method is not compatible with the value derived from the temperature of the Cosmic Microwave Background (CMB): this incompatibility, known as "Hubble tension" is one of the biggest problems of modern cosmology (Valentino et al. (2021). Currently, the last measurement of H_0 with SN Ia presented in Pascale et al. (2024) confirms using JWST the measurements performed with HST, establishing the tension and presumably excluding any

Figure 2. SN Ia object sn2020nlb in the host galaxy M85. Image taken with the Asiago Schmidt 67/92 telescope, INAF.

instrumental issue. In order to understand the nature of the tension, it is prominent to fully comprehend the nature of SN Ia; this is the main justification of the DWD study, since the exact formation channels of SN Ia are still not known.

The scenario involving two CO WD is called double-degenerate (DD), contrary to the single-degenerate scenario (SD) in which the supernova results from the He and H accretion of a CO WD from a non-degenerate companion star; eventually, the WD would reach the Chandrasekhar mass and burst into a SN Ia. As we shall see, these two cases are easily distinguishable by LGWA, so a correct characterization of the DWD population and the comparison with the observed SN Ia rate will discriminate the formation channel and the possible progenitors. Note that both the channels are probably present, especially taking into account the phenomenological variety of SN Ia events. Badenes & Maoz (2012), with observations based on the SDSS argue that the galactic DWD population is not sufficient to fully explain the observed SN rate ($r = (5.4 \pm 1.2) \cdot 10^{-3}$ yr^{-1}, Li et al. (2011)), but considering the sub-Chandrasekhar models in which a SN explosion can be achieved even without reaching the Chandrasekhar mass could help closing the gap. Both the scenarios benefits from indirect evidences, even if the DD scenario would better explain the lack of H and He emission in SN Ia spectra (Leonard 2007). In conclusion, there are still no strong evidences of the progenitor's nature.

LGWA offers a novel way to characterize short-period DWDs, hence probing this set of possible SN Ia progenitors from a new perspective. The GW carries a very different information set compared to the electromagnetic counterpart: other than a precise measurement of the period (and its changing rate), it is possible to determine the chirp mass $\mathcal{M}$ and, with less precision, the single component masses M_1 and M_2 (for the definition of these parameters, see sec. 3). With only these parameters it is possible to select the possible raw progenitor population as the subset with $M_1 + M_2 \gtrsim M_{Ch}$; further refinement can be done accordingly to the present SN Ia theories, resulting in a more refined population. These observations will allow to evaluate the abundance of such objects in our Galaxy and to compare the expected rate of DD merging events resulting from the probed population with the observed SN Ia rate. As we shall see, the expected detection horizon for LGWA for a reasonable SNR is well beyond the borders of the Galaxy, so we expect a nearly complete characterization of the short-period DWD galactic population, which is not possible with current optical surveys (electromagnetic in general) either for intrinsic properties, as the characteristic faint luminosity of WDs, spanning from $L \approx 10^{-1} L_\odot$ to $L \lesssim 10^{-5} L_\odot$ within the WD lifetime (Iben & Laughlin 1989) and the difficulties in the discrimination between single stars or binary systems, or extrinsic as the presence of the galactic centre that optically obscures the other side of the galactic disk and part of the bulge, where most of the oldest stars are located. As a result, even the most recent DWD optical surveys suffer from incompleteness and biases. On the other hand, if a sufficient precision in the localization of the DWD GW sources is reached, this would provide guaranteed multimessenger observations for the nearest systems, which would be observable in the with optical detectors, already knowing the binary nature of the systems and some of their parameters. The LGWA observations will clarify the physical processes involved in the last years of evolution of the DWDs, the interactions and many other aspects that are now not accessible with current detectors.

Resolving DWDs outside our galaxy would allow to have and independent calibration of the distances, hopefully directly shedding light on the problem of the Hubble tension. As shown in Del Pozzo (2014), it is indeed possible to measure the Hubble constant exploiting GW signals originating outside our galaxy: from a correct modelling of the GW signal and the geometry of the detector it is possible to get the luminosity distance and the sky localization of the source. For example, the event GW170817 as seen from LIGO/Virgo detector network (a binary neutron star merging) was estimated to be located within a 28 deg^2 sky area with a 90% confidence level, and at a luminosity distance of 40^{+8}_{-14} Mpc (Abbott et al. 2017). The localization capabilities of LGWA with respect to DWDs is thoroughly discussed in next sections, but since the signal can be integrated over the mission life period (10 years) for a typical DWD, the localization is expected to be very precise. Once located the position of the source, if the localization capabilities of the detector are sufficient it is possible to associate the signal to a specific galaxy, hence being able to correlate the optical redshift measured from that galaxy to the estimated luminosity distance, and thus providing a calibration for cosmological measurements. This method does not need the detection of the electromagnetic counterpart, but observing a SN Ia burst after the coalescence of a DWD system would further improve the parameter estimation, similarly to what has been done for the multimessenger event GW170817 by Radice & Dai (2019), since the constraints on some parameters coming from the counterpart observations (a better measurement of sky localization and distance for GW170817) would consequently lower the errors on the other parameters, like the single masses. Obviously, a multimessenger detection of a DWD that bursts into a SN Ia would directly prove the presence of the DD formation channel and test our knowledge of the use of SN Ia as standard candles. An estimation of the rate of these "golden events" is presented afterward. The opposite (GW detection without EM counterpart or EM detection without GW event) does not necessarily rule out the possibility of a DD event, as there are some models in which the deflagration happens a long time after the coalescence of the two CO WD (Shen et al. 2012). Furthermore, since this method does not require an electromagnetic detection, it would work for every source that could be precisely located, as binaries containing neutron stars and/or black holes, if the GW frequency lies in the LGWA range; however in the following I will focus only on the DWD population.

In conclusion, it is clear that the theoretical models and the experimental evidences are not strong enough to impose unequivocal

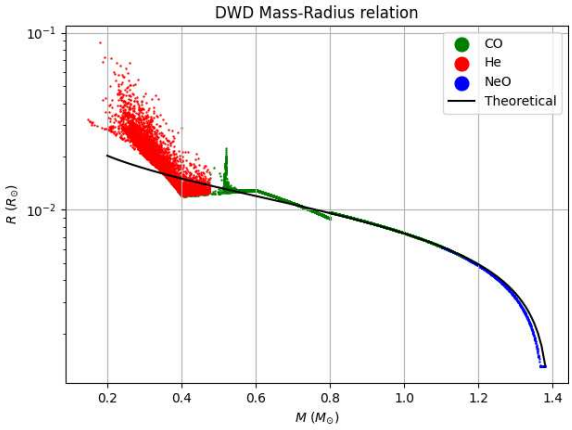

Figure 3. Mass-radius relation for a SeBa realization of a DWD population. Black line refers to eq. 1 with $\mu_e = 2$; it holds well above $0.8 M_\odot$, whereas at low masses the complete degeneration approximation is not satisfied, in particular near the surface.

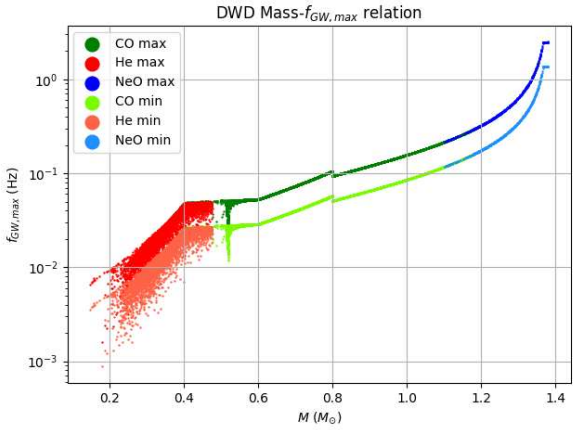

Figure 4. Mass-maximum frequency relation for the same population. The maximum frequency corresponds to a disruption at $d = 2R$, the minimun at $d = 3R$.

constrains to the DWD progenitors; thus the following simulation of LGWA capabilities regarding the DWD population is meant to be as wide as possible, without discarding any sub-population that could actually be detected.

2.3 Merging frequency for DWD systems

The small radius of WDs allows for a long GW-radiating phase, before other effects such as magnetic braking, Roche overflow and tidal disruption overcome. I now propose an quick analysis of the maximum GW frequency reached by a DWD system as a function of the WDs mass, considering $m_1 = m_2 = M$, eccentricity $\varepsilon = 0$ and WD radius $R_{\rm WD}$. Hydrodynamic simulations (Lorén-Aguilar et al. 2005) show that the merging occurs when the distance between the WDs is approximately $d \approx 2 - 3\ R_{\rm WD}$, by means of tidal disruption of the two WDs. This limit is heavily dependent on the physics of the merging process, and thus is not easily modelable with simple considerations; in this paragraph I present the possible extremes of the merging orbital separation, but in the following I will assume that the tidal disruption happens for $d = 2.5 R_{\rm WD}$.

The approximate maximum frequency reached by the system is than in the newtonian limit

$$\Omega^2 = (2\pi f)^2 = \frac{2GM}{d^3}$$

the GW frequency of the quadrupole mode is

$$f_{GW} = 2f = \sqrt{\frac{2GM}{\pi d^3}}$$

The mass-radius relation can be simulated by the population synthesis code SeBa (Portegies Zwart & Verbunt (1996), Toonen et al. (2012)) to better account for low-density regime effects: a DWD population with different masses is shown in fig. 3 with the simplistic theoretical prevision (eq. 1) for comparison. An accurate description of the SeBa usage is provided in sec. 5.2, but for now it is used only to simulate the mass-radius relation.

In fig. 4 it is shown the approximate maximum frequency reached before the merging. In particular, the He DWD population despite merging in the observable frequency band is less interesting, as the SN Ia progenitors are expected to be CO WD; in addition, the total mass does not exceed the Chandrasekhar mass (although, as I pointed out this is not a strong constraint). The CO DWDs, principal candidates for a SN Ia progenitor, merge at ≈ 0.1 Hz, namely the most sensitive frequency band of LGWA, where the horizon should be further than those of both LISA and ET. Note that this is a rough estimate, and the real maximum frequency depends on the complex dynamic of merging process, but it gives the order of magnitude of the merging frequency.

It is clear that in the SD scenario with a non-degenerate companion, the disruption of the companion star would happen for $d > R_\odot$ at least, leading to a merging frequency below the mHz and thus not detectable with LGWA.

3 THE BINARY SYSTEM GW EMISSION

The long observing period of LGWA mission, the natural behaviour of the response body (the Moon) that acts as an harmonic oscillator and the low frequency band make LGWA particularly suitable for the detection of long-lasting monochromatic sources. The main emitters are the compact binaries, as DWDs, NS-WD, NS-NS, NS-BH and BH-BH systems. These systems benefits from the absence of an atmosphere that mimes the gravitational energy loss, thus for a sufficient orbital separation the power dissipation occurs only via gravitational wave emission. In this section I will recall the relevant results concerning a binary system of two massive dots, which will be adapted to the physical situation in the following sections.

The system consists in two masses m_1 and m_2 separated by a distance d following circular orbits on the xy plane: for DWDs, a treatment of the eccentricity ε is not necessary (see sec. 5). In the keplerian limit, the slow inspiral of the system is describable as a

series of stationary circular orbits with orbital period

$$P = 2\pi\sqrt{\frac{d^3}{GM_{\rm tot}}}$$

The energy radiated from the system via GW emission is (Peters & Mathews 1963):

$$\frac{dE}{dt} = -\frac{32}{5}\frac{G^4}{c^5}\frac{m_1^2 m_2^2(m_1+m_2)}{d^5} f(\varepsilon) \tag{2}$$

Where G is the gravitational constant, c the speed of light and $f(\varepsilon)$ an eccentricity correction that reads $f(0) = 1$, so it will not be considered in the following. The result of this restriction is that the GW has only a quadrupolar component.

The energy of the keplerian system is $E = -\frac{1}{2}\frac{Gm_1m_2}{d}$, thus substituting $d(E)$ in the previous equation and solving for E it is possible to obtain $E(t)$ and thus $d(t)$. Using the period expression one eventually finds that the GW frequency, that is the double of the orbital frequency, is described by:

$$f_{GW}^{-\frac{8}{3}}(t) = f_0^{-\frac{8}{3}} - \frac{256}{5}\frac{G^{\frac{5}{3}}\mathcal{M}^{\frac{5}{3}}\pi^{\frac{8}{3}}}{c^5}\cdot t \equiv f_0^{-\frac{8}{3}} - \Delta(\mathcal{M})\cdot t \tag{3}$$

where f_0 is the GW frequency at $t = 0$, and $\mathcal{M}$ is the *chirp mass*

$$\mathcal{M} = \frac{(m_1m_2)^{3/5}}{(m_1+m_2)^{1/5}}$$

In the following the *GW* subscript is omitted to simplify the notation. Equation 3 is really important for the following, since it gives the frequency of the system after a certain time interval, or the time of the merging event starting from a given frequency and mass combination. The merging time t_m can be obtained by posing $f(t_m) = \infty$, since the frequency diverges at the merging. The time is thus simply

$$t_m = \frac{f_0^{-\frac{8}{3}}}{\Delta(\mathcal{M})} \tag{4}$$

Note that this expression is obtained in the Newtonian limit, so it is an approximation that is valid only for $d \gg 3R_{Sc}$, where the system become unstable for relativistic effects. This regime is not reached since the merging occurs well before, and the correction would be very small anyway.

Other important characteristics are the following:

- The energy radiated during the process reaches the maximum at the merging in a very short timescale. For the most of the time, the binary system emits a small amount of energy and behave like a nearly monochromatic source.
- The angle ι between the z-axis and the observer determines the polarization of the GW: for $\iota = 0$ the system is said "face-on" and the GW is polarized circularly (both the a_+ and $a_\times$ polarizations are present with equal intensity and a 90° phase shift), for $\iota = 90°$ the system is "edge-on" and the GW is polarized linearly. The observation angle heavily affects the detection of the system, and generally the best configuration is the "face-on".
- As highlighted before, these formulas are valid only as long as the system is describable in the classical mechanics limit: as the frequency reaches ∞, relativistic corrections are required. However for the study of DWDs this limit is not reached as the stars collide before. For this reason, eq. 3 is not valid above the frequencies calculated in sec. 2.3.

4 THE LUNAR GRAVITATIONAL WAVE ANTENNA

In this section is provided a general overview of the functioning of LGWA. As reported in sec. 4.2, the Moon is subject to deformations induced by the passing of a GW. These initial deformations cause the excitation of the normal vibrational modes of the Moon, seen as an elastic body. If the normal vibrations can be detected and correctly associated to a passing GW, it is possible to derive the characteristics of the GW that caused the particular observed excitation. The approach of using a large elastic body that can couple with the GW as an antenna, monitored by a readout system, was first theorized by Weber (Weber 1962) by using large aluminum bars as resonant bodies (Weber 1970) or the Earth itself (Weber 1967). None of these detectors have detected GWs: the resonant bars excitations couldn't reach a detectable amplitude, and the normal vibrational modes of the Earth that could be excited by GW are not usable because of the high spectral noise due to seismic activity. The use of the Moon as a response body is justified by the extremely low spectral noise, which enables the GW signal to be recognizable over the background.

A brief summary of the LGWA payload is presented in sec. 4.1; this section is not meant to be exhaustive, given the great complexity of the mission, but it will explain the main features of the detector necessary for the understanding of the general functioning of LGWA, and in particular the sensing mechanism. A complete description of the LGWA payload is contained in the LGWA White Paper (Ajith et al. 2024). In sec. 4.2 it is described the expected response of the Moon to a passing GW, using the normal-modes formalism, and the correspondent signal read by the LGWA inertial sensors. The complete response of LGWA to a GW is given by the coupling of these two elements, the seismometers as detectors and the Moon as an antenna.

4.1 LGWA mission payload

The core of the detector is a seismometer that consists in a suspended mass coupled with a readout system. I will refer to the whole seismometer with the acronym LIGS, for Lunar Inertial Gravitational-wave Sensor. The idea is to use the suspended mass as an inertial reference to measure the vibrations of the ground to which the seismometer is anchored. This is achieved through a double-pendulum configuration: the mass is suspended from one side with a pendulum and from the opposite side with a reverse pendulum, as illustrated in the schematics of fig. 5. In this configuration the mass acts nearly as it was free along the direction of suspension for small displacements around the equilibrium. In fact, for a normal pendulum the gravitational potential around the rest position can be expanded at the first non-zero term in an harmonic oscillator; considering the expansion of the potential for the double-pendulum configuration, one finds that the term of the second order is zero, namely the potential at the equilibrium goes as $O(\Delta x^3)$. Note that since at the equilibrium point the concavity changes its sign, the equilibrium is not stable and the dynamics around $x = 0$ is not oscillatory. This is not a problem since the signal does not come from an oscillatory motion of the mass: through the readout system a negative feedback system repositions the pendulum at $x = 0$ by applying a force to the mass, preventing it to move (with respect to the LIGS frame) by inertia. In this way, the mass is permanently locked in a small interval $x \in (-\varepsilon, \varepsilon)$, with

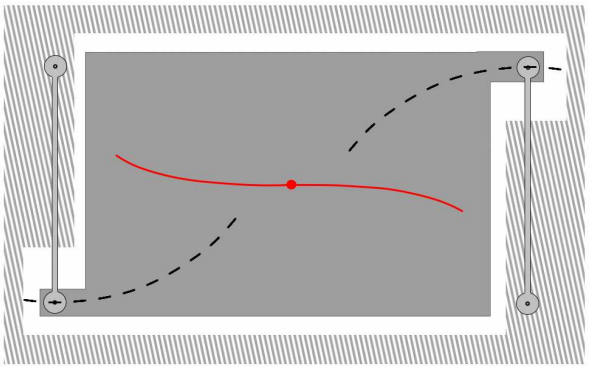

Figure 5. A schematics of the suspension of the test mass. The red line is the trajectory of the center of mass for this configuration, intentionally extended well beyond the working interval to highlight the cubic trend. The dashed frame is fixed to the structure of the LIGS and moves with the ground under the station.

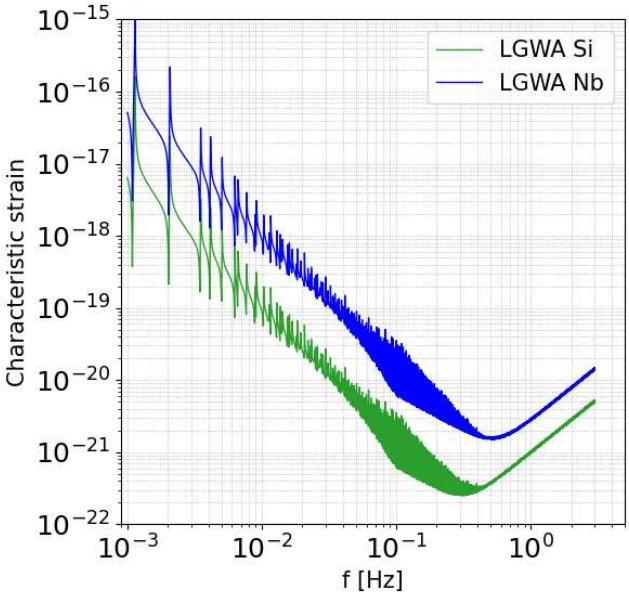

Figure 6. LGWA sensitivity: the characteristic strain on the y axis is obtained as $\sqrt{f \cdot \mathrm{PSD}}$, where PSD is the power spectral density that limits the detector's capabilities. The characteristic strain is adimensional since the PSD is expressed in Hz^{-1}.

a small ε determined by the sensitivity of the feedback mechanism, where the constant potential approximation is completely valid. The signal is thus the intensity of the force exerted by the feedback loop to maintain the mass locked in its position, and not the displacement of the mass.

As seen above, the lunar background seismic noise (BSN) is very weak, and this allows for the signal to stand out. In particular the frequency band in which LGWA will operate is approximately between 1 mHz and 4 Hz. This frequency band, despite containing plenty of interesting physical phenomena, would be poorly covered by the next generation GW detectors without LGWA: the terrestrial detectors (such as the planned Einstein Telescope, ET, and the Cosmic Explorers, CE1 and CE2) are strongly limited in the band $f \gtrsim 2$ Hz, and on the contrary the space-based detectors as LISA will operate with frequencies $f \lesssim 0.1$ Hz. LGWA will provide a bridge between these two frequency regimes, filling the in-between frequency gap. The operating band is obtained considering both the expected readout noise and the response of the Moon; the readout and feedback loop is planned to be realized with superconducting coils that act on the suspended mass via Meissner effects. The proof masses will be realized with Niobium or Silicon. The Silicon proof mass is expected to provide a more sensitive response (about 1 order of magnitude over the entire frequency band) as it is characterized by an higher mechanical quality factor, and it will be the model used in the simulations presented in sec. 6. With this assumption, the expected thermal noise will be the dominant component under 1 Hz, while above the readout noise is more important (Bi & Harms 2024). The LIGS should reach the sub-fm/$\sqrt{Hz}$ strain sensitivity in the band 0.1 - 1 Hz (van Heijningen et al. 2023), which means that over the radius of the Moon ($\approx 1.7 \cdot 10^6$ m) a relative strain sensitivity of $\approx 10^{-21}$ $\mathrm{Hz}^{-1/2}$ can be reached, as a rough estimate. The square of this sensitivity represents a measure of the power spectral density (PSD) of the overall noise that limits the detection. To obtain an accurate estimation of the sensitivity of the entire system (composed of the seismometers coupled with the Moon) over the entire frequency band, the LIGS sensitivity must be divided by the the Moon's strain response to a GW. The response is treated in sec. 4.2, and is characterized by a series of resonances below ≈ 0.1 Hz and a progressively smoother response above. Fig. 6 shows the sensitivity of the two options, measured by the Characteristic Strain parameter, namely the adimensional quantity $S_c = \sqrt{f \cdot \mathrm{PSD}}$. The rough estimation presented previously is correct, but an accurate model is crucial to exactly determine the detection capabilities with respect to specific GW sources (see sec. 6).

To reject the seismic noise and select only the effective GW signals, it is planned the deployment of four stations, each equipped with two LIGS for the two horizontal displacement measurement. In total the output of the detector will consist in 8 channels. The stations will be distributed in a star-like configuration whithin a range of some kilometers. The site of deployment will be a permanently shadowed region of the Moon, inside a crater at the South Pole, where the conditions of constant temperature $T \approx 40$ K create a thermally stable environment, reducing the corrections necessary to maintain the LIGS horizontally within a very small tolerance interval. In addition, to reduce the thermal noise and enable the use of superconducting elements for the feedback loop, the proof masses must be cooled to $T \approx 4$ K.

Finally, the LGWA mission presents several engineering difficulties that are under investigation, some of which are presented in the LGWA White Paper (Ajith et al. 2024), that include an effective noise cancelling, the levelling system, the design of the components and the electronics, the energy supply, the deployment of the array. These aspects do not directly affect the estimations of sec. 6 and are currently under development, so they are not treated here.

4.2 Response of the Moon to GW

Let $\vec{\xi}(\vec{r},t)$ be the displacement field of a response body (the Moon in the LGWA case) from the rest position, and $\vec{\chi}_N(\vec{r})$ the adimensional normal vibrational modes of the body, where N is a multiindex, namely a vector of indices, to which is associated a oscillation frequency ω_N and a quality factor Q_N. The normal vibrational modes are orthonormal in the sense of the following scalar product:

$$\langle\vec{\chi}_N|\vec{\chi}_{N'}\rangle = \frac{1}{M}\int_V d^3r\rho(\vec{r})\vec{\chi}_N(\vec{r})^* \cdot \vec{\chi}_{N'}(\vec{r}) = \delta_{N,N'} \tag{5}$$

Where the amplitude of the oscillation is weighted by the density of the point that oscillates. Note that these modes are not explicitly given to maintain the generality of the treatise, since it is expected that the real Moon eigenmodes can substantially differ from those of a uniform spherical elastic object. In the latter case, the modes are describable by the vectorial spherical harmonics, which can be taken as a rough approximant of the Moon modes if a more refined model is lacking.

Any small perturbation can be than univocally written as a sum of the normal modes, weighted by a dimensional coefficient $A_N(t)$ which has the dimensions of a lenght:

$$\vec{\xi}(\vec{r},t) = \sum_N A_N(t)\vec{\chi}_N(\vec{r}) \tag{6}$$

The problem of interest is to calculate the temporal evolution of the functions $A_N(t)$, given the $\vec{\chi}_N(\vec{r})$ set and the GW that perturbs the system. If the coefficients $A_N(t)$ are found, the response of the Moon surface is known and thus the displacement of the ground under the LIGS. In this formalism, the normal modes are the solutions of a diagonalized Hamiltonian of the whole system, which has been expanded in series around the equilibrium: as a result, the Hamiltonian takes the form of a sum of independent harmonic oscillators Hamiltonians, one for every eigenmode, each characterized by a resonant frequency ω_N, a quality factor Q_N that accounts for the energy dissipation and an equivalent mass for an harmonic oscillator, $\tilde{m}_N$. The single mode displacement $A_N(t)$ is a Lagrangian coordinate in this perspective. Every mode is than expected to follow a motion equation

$$\ddot{A}_N(t) + \frac{\omega_N}{Q_N}\dot{A}_N(t) + \omega_N^2 A_N(t) = S_N(\boldsymbol{h}(t)^{\text{gauge}}) \tag{7}$$

Where S_N is a scalar function that represents the perturbation induced by the GW. S_N is dependent on the the multi-index N, on the structural characteristics of the Moon (which are implicit in the construction of S_N) and has the GW tensor as the argument, along with the choice of the gauge in which the $h_{\mu\nu}$ tensor is expressed. Note that $h_{\mu\nu}$ is the small perturbation tensor to the Minkowsky metric tensor $\eta_{\mu\nu}$, namely the metric is given by

$$g_{\mu\nu}(t) = \eta_{\mu\nu} + h_{\mu\nu} \tag{8}$$

Different choices of the gauge lead to different explicit writing of the S_N function, depending of the meaning that can be attributed to the chosen gauge. Obviously, the overall expression of the perturbation $S_N(\boldsymbol{h}(t)^{\text{gauge}})$ is independent from the gauge. In the following two different gauges are considered: first, the most intuitive Lorentz gauge that can be interpreted as the Newtonian action of a passing GW on the Moon mass distribution, and than the TT gauge, in which the polarization of the GW is clearer. The first approach focuses on the properties of the Moon, while the second on those of the GW.

S_N has the meaning of a force, divided by the equivalent mass $\tilde{m}_N$ to give the dimensions of an acceleration, that is imparted to the amplitude A_N as an external forcing. The internal terms of dissipation and harmonic restoring force are accounted in the left member of the equation. The S_N term is thus meant to account for a mean of all the forces applied to every point of the mass distribution, that can contribute to a overall force applied to the amplitude of the entire vibrational mode. The forces must be weighed with the amplitude of the mode in the point where they are applied: for example, a force applied to a nodal point will not excite the mode at all, and so a force applied perpendicularly to the displacement vector of a mode. This tells that the weighting of the force must be done via a scalar product between the force and the displacement field of the eigenmode. In addition, since the modes are orthonormal, the sum of all these contributions over the multi-index N will return the entire force for every point, correctly accounting for the total action of the GW on the response body.

These considerations lead to the first approach, using the Lorentz gauge:

4.2.0.1 Lorentz Frame In the following the explicit formula for S_N in the Lorentz frame is derived using a Newtonian interpretation of the tidal force field exerted by the GW, with attention to the physical meaning rather than the exact formalism. If the reference system is chosen in the Moon's center of mass, the GW field exerts a tidal force on the mass distribution. For a system of free particles, the 3×3 matrix $h_{ij}(t)$, with i, j spatial indexes, resulting from considering only the spatial component of the tensor $h_{\mu\nu}$ and expliciting the time t as a parameter instead of a coordinate, determines the displacement of the particles with respect to the chosen reference frame. In particular, the displacement of a point mass from its rest position is given by

$$\vec{\zeta}(t) = \frac{1}{2}\boldsymbol{h}(t)\cdot\vec{r} \tag{9}$$

Where the displacement is proportional to the product matrix by vector of the GW matrix $\boldsymbol{h}(t)$ and the vector distance $\vec{r}$ from the origin. This is not true for an elastically bounded system, where every point's displacement is affected by the nearby points' displacements. Although, eq. 9 can be seen as the outcome of an apparent force dF that acts on every isolated mass $dM(\vec{r}) = \rho(\vec{r})d^3r$ producing an acceleration $\frac{1}{2}(\ddot{\boldsymbol{h}}(t)\cdot\vec{r})$. The force is apparent as the point is not subjected to a real acceleration in its reference frame, but from another reference frame the behaviour of this tidal displacement is not distinguishable from the displacement caused by applying a force

$$d\vec{F}(\vec{r},t) = \frac{1}{2}(\ddot{\boldsymbol{h}}(t)\cdot\vec{r})\rho(\vec{r})d^3r \tag{10}$$

This approach is valid also for an elastically bounded system, as the coupling between the GW and the mass distribution is mediated by a force exerted on every mass dM and not directly by a displacement field. The function S_N is thus obtained by integrating this force, weighting it as described previously via a scalar product with the mode amplitude. A normalization coefficient is included:

$$S_N(t) = \mathcal{N}\int_V \vec{\chi}_N(\vec{r})^* \cdot d\vec{F}(\vec{r},t) \tag{11}$$

Expliciting the local force as in eq. 10 one can obtain

$$S_N(t) = \mathcal{N} \int_V d^3r \rho(\vec{r}) \vec{\chi}_N(\vec{r})^* \cdot \left(\frac{1}{2} \ddot{\boldsymbol{h}}(t) \cdot \vec{r} \right) \tag{12}$$

Since the sum is weighted by the density $\rho(\vec{r})$, the normalization factor is $\mathcal{N} = \frac{1}{M}$. This is coherent with the physical meaning of the evaluation of the force applied to the amplitude A_N of the N-th eigenmode, with the dimensions required for S_N. This expression can be written in a more elegant form by using the scalar product previously defined:

$$S_N(t) = \left\langle \vec{\chi}_N(\vec{r}) \;\middle|\; \frac{1}{2} \ddot{\boldsymbol{h}}(t) \cdot \vec{r} \right\rangle \tag{13}$$

It is important to note that, solved eq. 7 with the forcing expressed by eq. 13, the quantity $\vec{\xi}(t)$ does not give the displacement signal measured by the inertial sensor mass, since the mass itself is subjected to the tidal force of the GW. The real signal is obtained by subtracting the displacement of the mass $\vec{\zeta}(t)$, found by using eq. 9, to the ground displacement $\vec{\xi}(t)$.

4.2.0.2 TT gauge While the treatise in the Lorentz frame has a very straightforward physical interpretation, the gauge hides some of the GW properties as the polarization. In the TT gauge the shape of the GW tensor is more clear, but S_N changes; it can be derived that S_N is described by the following expression:

$$S_N(t) = -\frac{1}{M} \int_V d^3r \; \vec{\chi}_N(\vec{r})^* \cdot \boldsymbol{h}^{TT}(t) \cdot \nabla \mu(\vec{r}) \tag{14}$$

where $\mu(\vec{r})$ is the shear modulus, a scalar field characteristic of the material. The shear modulus can be obtained by the velocity of the shear waves in the material v_T via $\mu = \rho v_T^2$. Due to the presence of the ∇ that acts on μ, wich contains the density ρ, this equation can not be immediately recast with the scalar product previously seen if the density is not constant.

Note that in TT gauge the dependence from the GW tensor follows directly from h^{TT} and not from its second derivative; In addition, the coupling with the normal mode happens by means of the contraction of h^{TT} with the shear modulus' gradient and not directly with a force that acts on the whole eigenmode.

Apart from these analytical models, for an accurate analysis of the LGWA data stream it will be necessary a more refined model that will account for the Moon's internal structure and the topography of the deployment site at various scales, as these factors are expected to heavily influence the propagation of the seismic waves that form the detectable signal. New techniques are being proposed (Bi & Harms 2024) to account for these effects, but the calibration problem is still complex and needs both numerical simulation models and seismic data from next lunar missions, including the proof-of-concept mission Soundcheck, that will test a simplified version of the LIGSs of LGWA.

5 GENERATION OF THE SYNTHETIC POPULATION

In order to simulate with accuracy the response of LGWA to the DWD population, inside and outside our galaxy, it is prominent to generate a reliable synthetic population. This is preferable as opposed to using the existing catalogues for many reasons:

- The intrinsic difficulties in detecting, observing the DWDs and accurately characterize the parameters of interest could introduce systematic biases in the analysis.
- Only a section of the galaxy has been thoroughly analyzed, for example by Gaia mission (Jackim et al. 2024); as a result, for example the bulge DWD population is not catalogued yet.
- The known short-period DWDs are very few, and not sufficient for a statistical analysis considering the frequency band of LGWA.

At the same time, the generation of a synthetic population presents considerable difficulties; in this section I'll explain the chosen procedure.

5.1 Population size estimation

In order to generate a realistic population, it is important to estimate the number of DWD systems in our galaxy. From now on, I will consider the DD scenario as the only formation channel for SN Ia; a mixed scenario (DD + SD) can be obtained simply by re-scaling the results. As previously anticipated, the the observed SN rate is $r = (5.4 \pm 1.2) \cdot 10^{-3}$ yr^{-1} (Li et al. 2011); I will now calculate the DWD population, as a function of the frequency, required to sustain this rate. I will consider r as constant: this approximation is valid on the timescales of the detectable DWDs (those characterized by a GW frequency above 1 mHz) because the time required to merge starting from $f_i = 1$ mHz is around 1 - 3 Myr depending on the masses, sufficiently small compared with the entire Hubble time (13500 Myr) to consider the SN Ia rate locally constant.

This normalization of the total population considers only the DWDs that will eventually merge after the inspiral. However, the final phases of the spiralling are quite complex and can result in different outcomes: other than the merging, there is the possibility of an outspiralling, caused by the mass exchange, that results in distancing the WDs. This event is expected to generate a complex waveform, for which an approximant is not available yet. Clarified this possible bias in the construction of the population, that will possibly lead to an underestimation of the total DWD number, the rest of the analysis is based on the simple hypothesis that every DWD with total mass $M > M_{Ch}$ will shrink, merge and produce a SN Ia event.

Let $\rho(f)$ be the DWD density in the frequency space, such that $dN = \rho(f)df$ is the number of DWDs with frequency between f and $f + df$. The merging of these dN systems will occur in a time interval $dt = t_m(f) - t_m(f + df)$, where t_m is the merging time derived in sec. 3:

$$t_m(f) = \frac{f^{-\frac{8}{3}}}{\frac{256}{5} \frac{G^{\frac{5}{3}} \mathcal{M}^{\frac{5}{3}} \pi^{\frac{8}{3}}}{c^5}} = \frac{f^{-\frac{8}{3}}}{\Delta(\mathcal{M})} \tag{15}$$

The merging rate is than

$$r = \frac{dN(f)}{dt(f)} = \frac{\rho(f)df}{t_m(f) - t_m(f + df)}$$

It follows that

$$\rho(f) = r \frac{t_m(f) - t_m(f + df)}{df} = -r \frac{dt_m(f)}{df} \tag{16}$$

f_m	f_M	expected
0.001	0.005	$(2.0 \pm 0.5) \cdot 10^4$
0.005	0.01	228 ± 62
0.01	0.05	42 ± 11
0.05	0.1	0.5 ± 0.1

Table 1. Expected population: the errors are calculated propagating both the error on the r estimation and the statistical dispersion of the $\Delta(\mathcal{M})$ function, drawn from the mass distribution of the convolved population obtained in sec. 5.3, considering only the systems with $M_{tot} > M_{Ch}$; As the errors are calculated from a mixed approach, they are only meant to indicative. In addition, for the last frequency interval non-gravitational effects overcome so the estimation could not be reliable.

Differentiating eq. 15 and substituting into 16 one obtains

$$\rho(f) = \frac{8}{3} r \frac{f^{-\frac{11}{3}}}{\Delta(\mathcal{M})} \tag{17}$$

which integrated in a frequency interval $I_f = (f_m, f_M)$ gives

$$N(I_f) = \frac{r}{\Delta(\mathcal{M})} \left(f_m^{-\frac{8}{3}} - f_M^{-\frac{8}{3}} \right) \tag{18}$$

The resulting expected population for various frequency intervals are listed in tab. 1.

Note that the influence of other effects at the merging time, which speed up the disruption process, does not affect the estimations regarding lower frequencies as it is simply modelable as a time shift in eq. 15.

5.2 Primordial population and evolution

Being the DWD parameter distribution poorly known, the present stellar population can be generated evolving a primordial population with the code SeBa[1] introduced in sec. 2. This code allows to completely simulate the evolution of a stellar population; in particular, for the sake of this analysis it is used to simulate a population of binaries in the parameter ranges that allow the formation of a DWD. The fundamental steps in the elaboration are:

- Sampling a population with given parameter distributions, implemented in the software. The parameters are the two star masses M_1 and M_2, the initial orbital separation, the eccentricity of the orbit, and the metallicity of the stars ϵ (the fraction of star matter that is not Hydrogen). All these parameters, with the exception of ϵ that is fixed for the whole population, are sampled accordingly with some distributions that can be chosen as input (initial mass function (IMF) for the primary mass, mass ratio for the secondary mass, orbital separation distribution and eccentricity distribution).
- Every binary system in the generated population is than evolved independently for a chosen time interval, taking into account all the major effects that contribute to the evolution of the single stars and the system as a whole.
- The output consists in a file that contains, for every system, the main evolutionary phases of the binary with all the parameters that describe the system: the time from the beginning at which the evolutionary step occurs, the orbital separation, the eccentricity, and for both stars the star type (from "planet" to "black hole", and all the other possibilities that stay in the middle), the mass, the temperature, the radius and the core mass.

[1] https://github.com/amusecode/SeBa

parameter	distribution	interval
Primary mass	Kroupa IMF	$0.95 M_\odot < M < 10 M_\odot$
Secondary mass ratio	Uniform	$0 < \frac{M_2}{M_1} \leq 1$
Orbital separation	Log-uniform	$1 R_\odot < d < 10^6 R_\odot$
Eccentricity	Thermal	$0 < \varepsilon \leq 1$
Metallicity		0.014

Table 2. Initial population parameters

The fiducial parameter distributions and parameter intervals are chosen accordingly to Korol et al. (2017) and reported in tab. 2. All the distributions are already implemented in the SeBa sampler. Despite effectively using a thermal distribution for the eccentricity, all the short-period DWDs have $\varepsilon = 0$ from the formation of the DWD, namely the end of the CE phase. Thus from now I will not consider the effects of eccentricity and work with circular orbits, as in sec. 3.

The resulting population consists in a sample of $2 \cdot 10^6$ binary systems, each with its evolutionary history, with a overall initial mass of $5.8 \cdot 10^6 M_\odot$. A fraction of $\approx 75\%$ of the systems becomes DWDs at some point of the evolution (these systems are shown in fig. 7), $\approx 5.8\%$ of these experience a short-period phase before present time, and only some tens fall in the LGWA frequency band exactly at the end of the 13500 Myr period, all around the mHz and none above 10 mHz. It is clear that this single burst cannot provide a statistical sample of the population, since the expected DWD galactic population in the mHz should account for $\approx 2 \cdot 10^4$ systems above the Chandrasekhar mass in order to reproduce the current SN Ia rate (see tab. 1), and the simulation can't reproduce at all the rare but crucial population with $f_{GW} > 0.01$ Hz in the most sensitive band of LGWA.

The solution comes from using the generated population as a δ function and convolve it with a chosen star formation history (SFH). For every t, 0 Myr $< t <$ 13500 Myr, in the population a certain number of new systems are formed (systems/year); it is thus possible to define a formation rate $R_{\mathrm{SFH}}(t) \in [0, 1]$ by normalizing the SFH of the population at the value that it reached at the peak of star formation. For the time interval $(t, t + \delta t)$ a fraction $R_{\mathrm{SFH}}(t)$ of the whole SeBa population is sampled and the frequency is evaluated at the present time, namely at the time $\tilde{t} = 13500$ Myr $- t + \xi \cdot \delta t$ in the simulation. The parameter ξ is drawn randomly from the interval $(-0.5, 0.5)$ for every system to account for a uniform distribution within the minimum period δt, and thus smoothing the single δ functions into a continuous distribution. I will discuss later the choice of the time resolution δt. If the algorithm finds a system that for $\tilde{t}$ lies in the LGWA frequency band, the system is added to the convolved present population. In addition, let M_s be the "total simulation mass", namely the sum of the masses of the stars at the time of formation ($\tilde{t} = 0$); this characteristic mass is used in sec. 5.3 to correctly account for the various stellar populations within the MW. This is the most reliable estimation of the convolved population mass, even if it does not represent the effective mass at the end of the evolution. Obtaining this second estimation would require the complete simulation of the

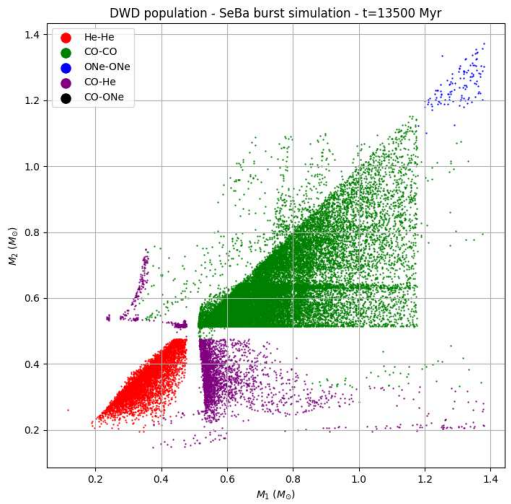

Figure 7. δ population at $t = 13500$ Myr. M_1 refers at the most massive star at the formation of the binary ($t = 0$).

entire population evolution, which is not reasonable considered the necessary computing power.

This approach completely solves the initial problem as not only the few short-period DWDs that remain at $t = 13.5$ Gyr are considered, but all the systems that at some point of the 13.5 Gyr evolution had become a DWD. In this way the computationally expensive SeBa simulation is better exploited. In addition, the δ-convolving approach benefits from two main virtues:

- A SFH is naturally simulated with accuracy as the convolution of any function (as the chosen $R_{\rm SFH}(t)$) with a Dirac δ gives the function itself; this allows to test multiple SFH hypothesis without running the SeBa simulation (extremely computationally expensive) a great number of times, but only one long run to generate the δ burst ($\approx$ 200 hours of CPU have been used). In addition, different galactic components have different SFHs, hence this approach is ideal to simulate a complex galactic structure.
- A large DWD population can be easily produced, even larger of the actual population, allowing for more precise statistical considerations. This could not be possible with direct evolution simulation, given the extremely low percentage of observable systems in the total population.

However, there are some drawbacks that must be taken into account:

- The δ burst refers to fixed initial parameters that could change over time in the real SFH. For example, the metallicity is expected to increase as the galaxy ages or vary for the different galactic populations (bulge, thin disk, thick disk, see sec. 5.5), but this effect cannot be taken into account since a variation in the metallicity would require to re-run the evolutionary simulation. The same is true for the IMF.
- The same DWD system is counted more than once if δt is small enough, resulting in a certain degree of correlation inside the population.

For the former there is not a simple solution, and it will contribute for some degree of systematic error. This problem however is strongly mitigated by the choice of the SFH: in general, it is expected that $R_{\rm SFH}$ in the early stages of galaxy evolution is far higher than in the late stages (sec. 5.3); this results in a shorter effective formation period, that is more acceptably modelable with fixed metallicity and IMF function. In addition, it is worth noting that other systematic effects could be more important, as the partial decoupling of the initial stellar population from the position within the galaxy. This particular aspect is discussed in sec. 5.5.

For the latter, it is important to estimate how much time a system remains in the LGWA band. An upper limit is found using the expression for the time to merge for a binary system, eq. 15. The initial frequency for which the algorithm recognizes the DWD as detectable with LGWA is $f_i = 1$ mHz. The resulting merging times for the typical DWD masses is around 1 - 3 Myr. This means that the time resolution δt should be lower than 1 Myr, otherwise some systems would be lost in the process, but not too low to cause detectable correlation in the population. Note that lowering δt is desirable, as doing so the resulting population would increase in number. A lower limit for δt can be found imposing that the frequency space density generated by the repetition of one system should be lower than the density of different systems. This constrain prevents the formation of isolated "clusters" or "streaks" in the frequency space due to the multiple counting of a single system. With really rough estimations (considering one half of the systems in the interval 1-5 mHz and imposing there the condition, since the low-frequency band corresponds to a slower evolution) it is found that this limit $\delta t_{\rm min}$ always lies under 0.001 Myr. The accurate limit must be even lower, since all the approximations are for the excess, but even this value is too low for a reasonable elaboration time. Lastly, the bigger is the initial SeBa sample, the higher will be the different-systems density and thus the smaller the minimum δt, so the maximum potential size of the convolved population grows faster than linearly with regards to the SeBa population size.

In conclusion, for the chosen initial population size, taking $\delta t \in [0.01, 1.0]$ Myr is a legitimate choice that does not introduce a significant correlation while exploiting at the best the DWD systems that had been previously elaborated.

5.3 Star Formation Histories

Once generated the δ population sample, the final population is generated via the convolution with a chosen SFH. The spatial distribution of the DWDs (see sec. 5.5) needs to be performed considering distinct components of the total galactic population; in particular, for the bulk of the galaxy a bulge + disks model is used. In addition, also other stellar populations could be simulated, as the Magellanic clouds, the globular clusters, and finally other galaxies within the horizon of LGWA, to completely model its detection capabilities. However, for this analysis I will develop an accurate model for the MW and reuse the generated population to model the extragalactic DWD population. In the following, to account for the different SFH that generated the MW sub-populations, various $R_{\rm SFH}$ are consid-

ered and commented. Afterwards, different hypothesis are presented on the combination of the single populations to obtain the galactic model.

5.3.0.1 Constant formation The most simple model consists in a constant star formation rate (SFR) $R_{\rm SFH}$ from $t = 0$ to 13.5 Gyr. As the DWD production is uniform in time, this model would automatically match the calculated population density distribution as a function of the frequency (eq. 17), since the corresponding merging rate is also uniform. This can be a good model for the disk component of the MW.

5.3.0.2 Exponentially declining Another SFH model, used by Korol et al. (2020), prescribe an exponentially declining SFR, with a characteristic time of 5 Gyr. Given the long decaying timescale, this could be a more refined model for the disk, instead of the constant formation.

5.3.0.3 Burst The star formation occurs in a very short period (≈0.5 Gyr) of evolution. The burst is modeled as a gaussian function. This SFH is meant to model an old population that after an initial burst did non experienced other formation phases if the burst occurs at the beginning (note that since the short-period DWDs are expected to already form at relatively high frequency and evolve fast, this type of SFH is likely to produce a thinner DWD population), or a major star production event that happened subsequently.

5.3.0.4 Bulge model A model developed specifically for the MW bulge by Haywood et al. (2016) is approximately describable with a constant SFR R from $t = 0$ to $t = 9$ Gyr, and another phase with increased SFR $R' = 3R$ from $t = 9$ Gyr to $t = 13$ Gyr.

5.3.1 Milky Way components

An agreement on which SFH better represent the various MW components is far from being reached in literature: while some prescribe an increasing SFR in the disks (Snaith et al. 2015), others (Vergely et al. (2002) and Cignoni et al. (2006)) hint at a decreasing SFR with a major star production around 2 - 3 Gyr. The models commonly used for the source abundancy estimations (Korol et al. 2020) use initial burst, constant formation and exponentially declining SFHs. Regarding the bulge, an opposite model with regards to Haywood et al. (2016) is presented by Ferreras et al. (2003), with a star formation concentrated in the 2 - 3 Gyr interval instead of 9-13 Gyr.

Among the recent modeling of the disks, Fantin et al. (2019) present a SFH for the two disk components, with a constant SFR for the thin disk from $t = 0$ to $t = 9$ Gyr and a burst formation of the thick disk at $t = 9.8$ Gyr, modeled as a gaussian with $\sigma = 0.5$ Gyr. This model accounts for the separate formation of the thick disk after a merging event (Helmi et al. 2018), and being based on WD observations it could reproduce more realistic results on the simulated DWD population. Other evidences from Gaia (Mor et al. 2019) show an exponentially declining SFH instead of a constant SFR in the first 9 Gyr, with a less pronounced thick disk burst. For these reasons, he fiducial model for the thick disk is chosen to be a gaussian burst at $t = 9.8$ Gyr with $\sigma = 0.5$ Gyr, while for the thin disk the constant and exponential models will be compared.

The DWD relative abundance among the components is chosen comparing the mass of the simulations $M_{s,\rm bulge}$, $M_{s,\rm thin}$, $M_{s,\rm thick}$ with the estimated masses reported in tab. 4, therefore there is not the problem of weighting the SFHs of the various components via the multiplicative density coefficients.

The ratio between the population masses is obtained by properly sampling the convolved populations. Let χ_b, χ_t, χ_T be the three sampling coefficients, and N_b, N_t, N_T the number of super-Chandrasekhar binaries in the convolved simulations, respectively for the bulge, the thin disk (either constant or exponential SFH) and the thick disk; by imposing the ratio constrains on the masses:

$$\frac{\chi_t M_{s,\rm thin}}{\chi_T M_{s,\rm thick}} = \frac{M_{\rm thin}}{M_{\rm thick}}$$

$$\frac{\chi_t M_{s,\rm thin}}{\chi_b M_{s,\rm b}} = \frac{M_{\rm thin}}{M_b}$$

and the total number of super-Chandrasekhar DWDs:

$$\chi_t N_t + \chi_T N_T + \chi_b N_b = N_{tot}$$

it follows that

$$\chi_t = \frac{N_{tot}}{N_t + N_T \dfrac{M_{s,\rm thin} M_{\rm thick}}{M_{s,\rm thick} M_{\rm thin}} + N_b \dfrac{M_{s,\rm thin} M_{\rm b}}{M_{s,\rm b} M_{\rm thin}}}$$

$$\chi_T = \chi_t \frac{M_{s,\rm thin} M_{\rm thick}}{M_{s,\rm thick} M_{\rm thin}}$$

$$\chi_b = \chi_t \frac{M_{s,\rm thin} M_{\rm b}}{M_{s,\rm b} M_{\rm thin}}$$

where the simulation masses and N_x are listed in tab. 3. To compute the sampling coefficients is used $N_{tot} = 2 \cdot 10^4$ after the estimations presented in sec. 5.1.

Once the two SFHs scenarios for the thin disk are simulated, one is to be chosen for further elaboration: the main difference is not in the composition of the population (masses distribution and frequencies) but in the number of short-period DWD systems compared with the total mass: for the constant SFH the DWD abundance is ≈ 20% higher compared to the exponential SFH. This results in increased sampling coefficients χ_b and χ_T in the case of exponential SFH, and a consequent redistribution of the DWDs in the MW components to match the total number. The resulting SN Ia rate is shown in fig. 8, and only minor differences are expected between the two scenarios before 2.5 Myr from now. The exponential SFH seems to produce a slightly more stable SN Ia rate in a time interval of 2 Myr; lacking other strong motivations to chose between the SFHs, in the following the exponential SFH is used as fiducial model, accordingly with the estimations from Gaia data (Mor et al. 2019). In any case, the similitude between the populations makes this choice less relevant. The parameters distribution of the three populations are presented in fig. 9.

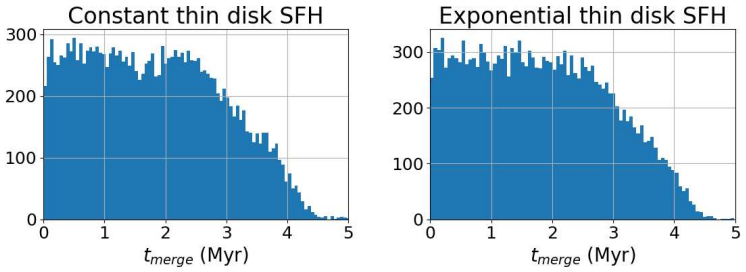

Figure 8. The overall galactic SN Ia rate from the two possible populations (constant or exponential SFH for the thin disk). Every bin corresponds to $5 \cdot 10^4$ yrs.

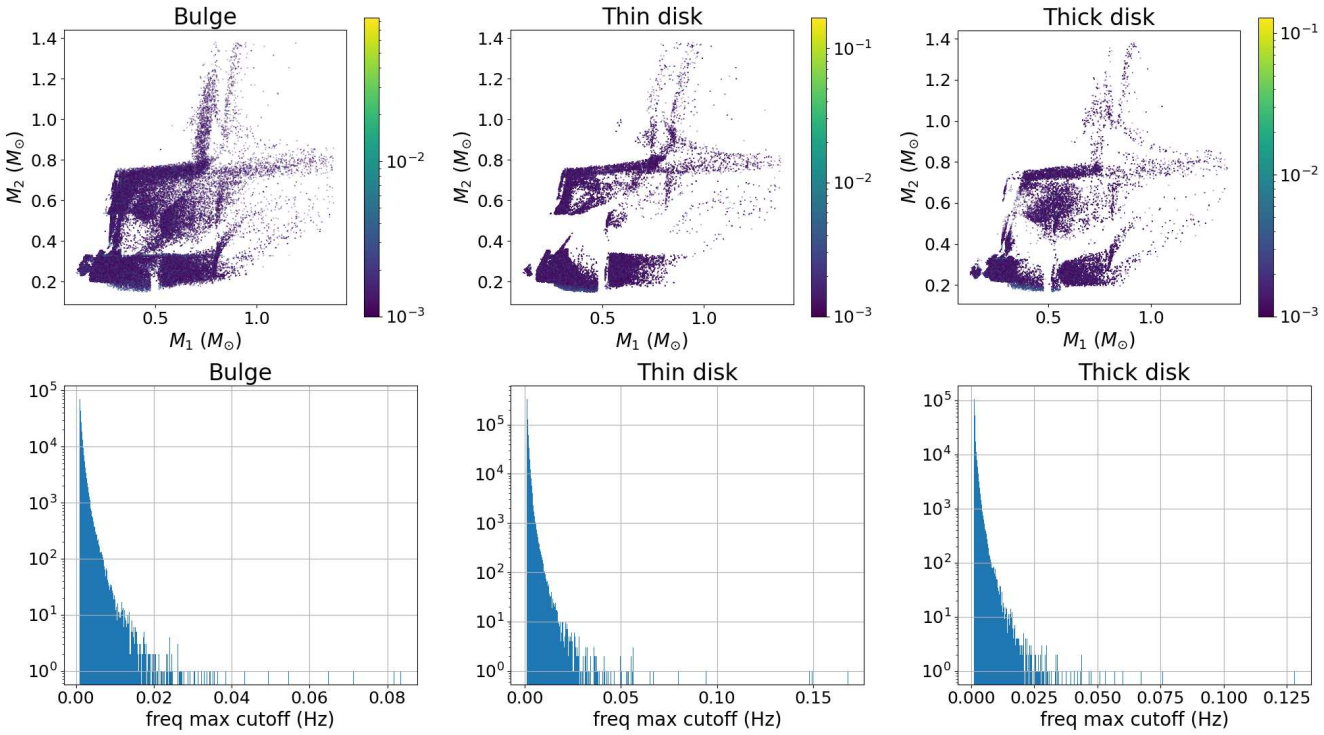

Figure 9. The three population components of the MW, with the SFHs and the relative abundances described in sec. 5.3. Up: M_1 vs M_2 scatter with max cutoff frequency colorbar. Down: max cutoff frequency histograms.

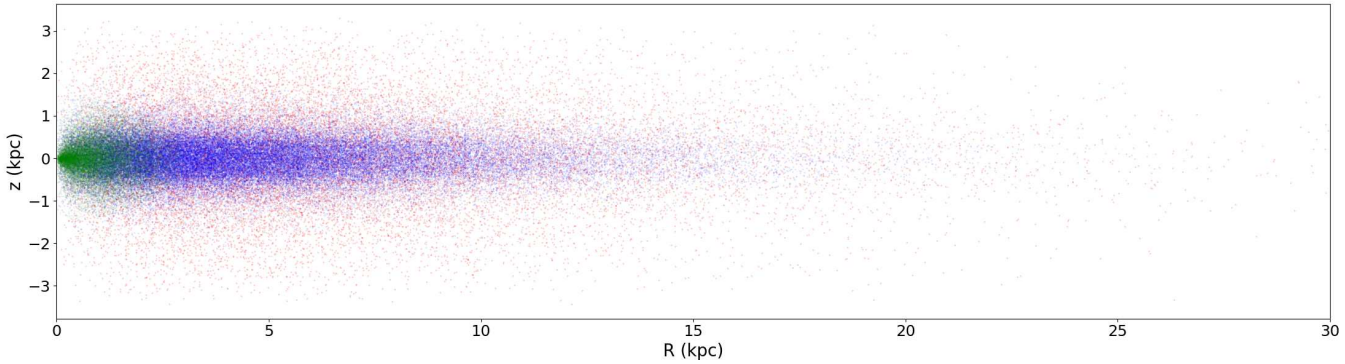

Figure 10. z - R projection of the MW components model, with the relative abundances obtained from DWD count. Only 10% of the objects are shown.

component	δt (Myr)	simulation mass ($M_\odot$)	$N_{>\mathrm{Ch}}$
Bulge	0.3	$1.35 \cdot 10^{11}$	71835
Thin disk (constant SFH)	0.2	$2.62 \cdot 10^{11}$	56144
Thin disk (exponential SFH)	0.2	$1.22 \cdot 10^{11}$	22518
Thick disk	0.1	$7.31 \cdot 10^{10}$	27049

Table 3. Convolved populations characteristics

5.4 Other parameters

The complete GW analysis, performed with the code GWFish, needs also other parameters, either extrinsic or less important than the parameters previously discussed:

- System inclination: the inclination θ of the system is an extrinsic parameter that is chosen with an uniform distribution in $\cos\theta$.
- Polarization angle: ψ is chosen uniformly in $(0, 2\pi)$.
- Phase: the initial phase of the waveform is not important for long-period observations, however it is chosen uniformly in $(0, 2\pi)$.
- a_1 and a_2: components of the WDs spins along the orbital angular momentum, in units of M^2, where M is the WD mass, in natural units; this parameter is chosen uniformly in $(0, 0.1)$, and plays a negligible role in the definition of the overall waveform.

5.5 Spatial distribution within MW

The mass distribution of the MW is still matter of debate, and growing evidences show that the structure of the galaxy is very complex (Di Matteo 2016). The accurate sampling of a realistic structure would however be difficult to implement, and wouldn't lead to great improvement in the estimations: in the modeling some rough approximations have been already introduced, as the constant metallicity. The adopted model will thus be quite simple, despite correctly considering the overall distribution of the stellar population.

I adopt a model consisting in a central bulge, a thin disk and a thick disk. In the following I will use a cylindrical coordinate system, with the origin in the galactic center of mass, the z-axis as the galaxy's rotational symmetry axis, $R = \sqrt{x^2 + y^2}$ the radial distance from the z-axis and θ the angular variable. The model is thoroughly described in McMillan (2017); in addition to being accurate, it is also easily implementable in a sampler thanks to the analytical form of the stellar densities. The used parameters are listed in tab. 4.

The bulge is modeled through the distribution:

$$\rho_b(r) = \frac{\rho_0}{(1 + r'/r_0)^\alpha} \exp\left[-(r'/r_{\mathrm{cut}})^2 \right] \tag{19}$$

with $r' = \sqrt{R^2 + (z/q)^2}$, while the disk density is the sum of two parts: the thin disk and the thick disk, each parametrized with:

$$\rho_d(R, z) = \frac{\Sigma_0}{2 z_d} \exp\left[-\frac{|z|}{z_d} - \frac{R}{R_d} \right] \tag{20}$$

To perform the elaboration, only $r' < 3$ kpc for the bulge and $R < 35$ kpc for the disks are considered. Despite being distinguishable by the chemical composition, I will use this double disk modeling only to account for a better spatial distribution, and the chemical composition will not affect the simulation of the convolved population, as said before.

The central density ρ_0 of the bulge and the surface densities Σ_0 are used to chose the ratio between the bulge and the disk populations and not to compute the effective total mass. The total number of DWD will be normalized to match the observed SN Ia rate, in the hypothesis that all the SN Ia come from the DD channel. The resulting spatial distribution, obtained using a dedicated sampling code, is represented in fig. 10.

parameter	value	meaning
ρ_0	$9.93 \cdot 10^{10} M_\odot$ kpc^{-3}	central bulge density
r_0	0.075 kpc	bulge radius for algebraic decrease
r_{cut}	2.1 kpc	bulge radius for exponential cut
α	1.8	algebraic decrease exponent
q	0.5	z semiaxis oblation of the bulge
$z_{d\mathrm{thin}}$	300 pc	scaleheight of the thin disk
$z_{d\mathrm{thick}}$	900 pc	scaleheight of the thick disk
$R_{d\mathrm{thin}}$	2.53 kpc	scalelenght of the thin disk
$R_{d\mathrm{thick}}$	3.38 kpc	scalelenght of the thick disk
$\Sigma_{0\mathrm{thin}}$	887 $M_\odot$ pc^{-2}	thin disk central surface density
$\Sigma_{0\mathrm{thick}}$	157 $M_\odot$ pc^{-2}	thick disk central surface density
M_b	$8.9 \cdot 10^9 M_\odot$	total mass of the bulge
M_{thin}	$3.5 \cdot 10^{10} M_\odot$	total mass of the thin disk
M_{thick}	$1.0 \cdot 10^{10} M_\odot$	total mass of the thick disk

Table 4. MW parameters from McMillan (2017)

5.6 Extragalactic sources: spatial distribution and DWD populations

While for the MW the populations are distributed following a complex spatial model, for the extragalactic sources this becomes superfluous for the objectives of this analysis: as the distance of a galaxy becomes larger than its characteristic sizes, the spatial distribution of the population does not play anymore a significant role in determining the detectability and the parameter estimation of the single DWD. Instead of a complex spatial distribution, these sources are associated directly with the position of the whole stellar population in ICRS coordinates (d luminosity distance from Sun, α and δ ra and dec respectively).

The data describing the galaxies is drawn from the HyperLeda[2] catalogue (Makarov et al. 2014). In particular, I used the following data for all the galaxies within 35 Mpc:

- Position: ra, dec and distance modulus m_{best}, which is related to the luminosity distance d_l through the relation

$$m_{\mathrm{best}} = 5 \log(d_l) + 25$$

This relation is used to compute the luminosity distance of the galaxy. As a note, the parameter m_{best} is obtained as a weighted average two different measurements of the distance modulus: m_z, which is measured using the redshift and is more important at higher distances, and m_0 which is obtained with independent methods, and is more reliable on small distances. For further details, refer to http://leda.univ-lyon1.fr/.

- B-band magnitudes: the apparent magnitude m_B in the B band corrected for extinction, and the absolute B magnitude M_B. These parameters are used to compute the galaxy colour (along with the K

[2] http://leda.univ-lyon1.fr/

apparent magnitude) and the SN Ia rate (see below). Note that the extinction correction is necessary since the major absorption occurs in the bluer band of the optical spectrum.

- K-band magnitude: the apparent magnitude m_K is used to compute the $B-K$ colour. Since the K band refers to the near-infrared spectrum, which is nearly not affected by the dusts, an extinction correction is not provided.
- Morphological type of the galaxy, expressed in the Hubble morphological classification. This parameter is used to obtain the SN Ia rate in the case that the colour is not available (in particular when the K band lacks, which occurs for a not negligible fraction of the population).

The SN Ia rate is than obtained using the rate-size relations described in Li et al. (2011). In particular, two parameters are necessary to accurately describe the rate in a galaxy, one chosen between the morphological type and the $B-K$ colour, and the other from the B-band luminosity, the K-band luminosity or the stellar mass. Given the HyperLeda data, I chose to calculate the rates preferably from the $B-K$ colour (obtained simply by $m_B - m_K$) and the B band luminosity, and where this was not possible for the lacking of the K apparent magnitude I used the morphological type and the B band luminosity. The luminosity is calculated with

$$L_B = 10^{-0.4(M_B - M_\odot)} L_\odot \tag{21}$$

where M_B is the absolute corrected B-band magnitude, $M_\odot = 4.8$ is the absolute magnitude of the Sun and $L_\odot$ is the luminosity of the Sun. The B luminosity is than expressed in units of $10^{10} L_\odot$ as a common scale unit for the luminosity of galaxies.

The galaxies that do not have neither of these two sets of data represent a very small component, which consists mainly in negligible stellar aggregates, and is not expected to play a significant role in the overall SN Ia rate outside the MW. Thus these systems are directly discarded.

The rate-size relations that relate the B band luminosity and galaxy colour or morphological type to the rate r are in the form of power laws:

$$r(\text{type}, L_B) = \text{SNuB}(\text{type}, L_0)\left(\frac{L_B}{L_0}\right)^{1+RSS_B} \tag{22}$$

$$r(B-K, L_B) = \text{SNuB}(B-K, L_0)\left(\frac{L_B}{L_0}\right)^{1+RSS_B} \tag{23}$$

Where SNuB is a rate for an average size galaxy with luminosity $L_0 = 10^{10} L_\odot$ and is dependent from the colour or the morphological type, and RSS_B is a power-dependent correction to the simple linear relation between the size (expressed as a luminosity) and the rate. The average-size SNuB coefficients and the relative RSS_B for the different colour and morphological types bins, drawn from Li et al. (2011), are listed in tab. 5. The resulting rates are expressed in units of one SN Ia every 100 years. A plot of the positions of the galaxies, with the corresponding rates and distances, is shown in fig. 11.

The estimation of cumulative SN Ia rate within 10 Mpc is 15.4 SN/100 yrs, which is found to be compatible with the estimation obtained from the volumetric local SN Ia rate of $3.01 \pm 0.62 \cdot 10^{-5}$ SN Mpc^{-3} yr^{-1} (Li et al. 2011), which implies a cumulative rate of 13 ± 3 SN/100 yrs for a 10 Mpc horizon. Note that since the MW is located in an overdensity, the SN volumetric rate is expected to decrease with higher volumes, which is the reason of such choice of the verification volume.

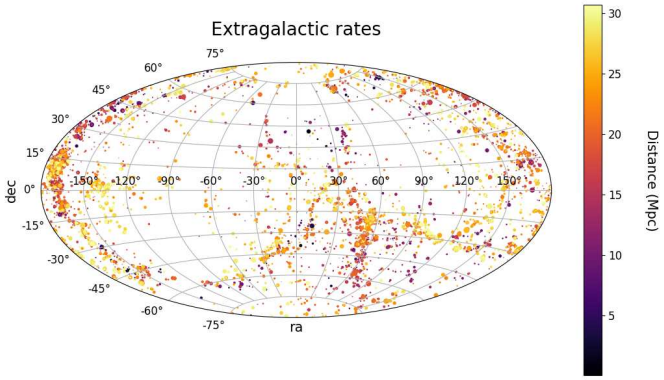

Figure 11. Extragalactic population: the plot shows the position of the galaxies from the HyperLeda catalogue; the colorbar indicates the luminosity distance, and the size of every dot represents the rate associated with the relative galaxy. For graphical clarity, the size s of the markers are related to the SN Ia rate r through the relation $s \propto \log(r+1)$. It is evident that along the galactic plane there is an incompleteness of the actual galaxy population.

Hubble type	SNuB(L_0)	RSS_B	$B-K$	SNuB(L_0)	RSS_B
E	0.305	-0.23	<2.3	0.158	-0.25
S0	0.282	-0.23	2.3 - 2.8	0.152	-0.25
Sab	0.271	-0.23	2.8 - 3.1	0.231	-0.25
Sb	0.217	-0.23	3.1 - 3.4	0.248	-0.25
Sbc	0.198	-0.23	3.4 - 3.7	0.260	-0.25
Sc	0.200	-0.23	3.7 - 4.0	0.250	-0.25
Scd	0.165	-0.23	>4.0	0.305	-0.25
Irr	0.000	-0.23			

Table 5. SNuB coefficients for the rate calculation. The reference B-band luminosity is $10^{10} L_\odot$.

Considered that the population that can be detected from LGWA outside our galaxy consists only in the most massive and short-period DWDs (see sec. 6), only super-Chandrasekhar systems with $f_{\text{cutoff}} > 0.005$ Hz are considered. For every galaxy, the associated number of systems is determined with eq. 18 on the frequency band $(0.005, 1)$ Hz, similarly to what has been done for the MW population: the total number of DWD binaries can be simply obtained by multiplying the rate (in units of SN/100 yrs) for the constant 498 (in units of 100 yrs) that results from the integration in the frequency space (eq. 18).

The DWD population used to build the extragalactic sources is derived from the super-Chandrasekhar sub-population of the MW via an amplification process: since the expected overall population is much bigger than the synthetic MW population, to not repeat the exact same systems multiple times over the extragalactic population a random process is applied to 5000 copies of the initial MW population:

- The masses are randomly changed within $0.01 M_\odot$
- The system is evolved for a random time $t \in (0, 10^5)$ years.

This does not affect the general shape of the population, since it can sustain a constant merging rate for 2 Myrs (see fig. 8).

- The new parameters (frequency cutoff and geocent time) are calculated for the new system, if the DWD did not merge before.

The resulting population consists in $\approx 2 \cdot 10^5$ systems, that is enough to provide the $1.5 \cdot 10^5$ systems required to sustain the total rate within 30 Mpc.

The population is than completed with the remaining parameters as described in sec. 5.4. The resulting semi-synthetic catalogue consists in approximately 148000 objects within 30 Mpc, and 7650 within 10 Mpc.

5.6.1 Error budget on extragalactic population

It is important to note that the population that has been produced could suffer from some errors: I will now list the most important, with a correspondent estimation of the relative error induced on the synthetic population.

- Statistical sampling: given the high number of sampled parameters and the relative small number of the systems in the overall population, the population is subject to great variations if the sampling is repeated. This behaviour is modelable with a Poisson statistic over the bins in which the systems will be sorted at the end of the elaboration (such as SNR bins, sky localization bins, excetera, see sec. 6). The casual error associated with every bin containing N system is than taken equal to $\sqrt{N}$, accordingly with the chosen statistic.
- Incompleteness of the HyperLeda catalogue: as shown in fig. 11, it is not possible to identify the galaxies that are behind the galactic plane; this will cause a systematic underestimation of the sources that will be visible to LGWA even if obscured by the MW disk for electromagnetic observations. This systematic error does not exceed the 25% of the total population: this percentage represents an estimation of the Zone of Avoidance caused by the obstruction of the MW (Kraan-Korteweg & Lahav 2000). The total systematic error can be taken between 20% and 25%.
- Errors in the estimation of the rate: all the parameters used for the estimation of the SN Ia rate (reported in tab. 5) are subjected to moderate errors for SNuB, of approximately 5%, and large errors for the corrective parameter RSS_B, around 60% – 90%. This is due to the limited amount of SN Ia that can be used to calibrate this data. A safe estimation for the error introduced by the parameters is taken to be about 10% of the total rate.
- Errors in the HyperLeda data: generally negligible when confronted with the previous sources of error; the major error source is the estimation of the distance and the colour, which can be distorted by the extinction. Since a correction for the extinctions is already given in the catalogue, this is not considered as a significant systematic source of error.

6 POPULATION ANALYSIS

The analysis of the population generated in the last section is performed by the code GWFish (Dupletsa et al. 2023). This tool allows for accurate simulation of the response of a GW detector to a signal characterized by the parameters simulated in sec. 5.

Let $d_\theta(t)$ be the signal stream from the detector, that consists in a real GW signal modelled by an approximant $h_\theta(t)$ that depends on a parameter set $\{\theta_i\}$, over a stochastic gaussian noise $n(t)$. The GW signal $h_\theta(t)$ is obtained from the tensor h_{ij} by contracting it with a response tensor $\mathcal{A}^{ij}$ that represents the sensitivity of the detector. Note that the tensor $\mathcal{A}^{ij}$ is a function of time, as the detector is moving over time (with the Moon around the Earth and the Sun for LGWA). For short-time signals this variation is negligible, but since a DWD observation is obtained by integrating the signal over the entire mission lifetime this effect must be considered. The calculation of the response tensor is implemented in GWFish. The parameter estimation (PE) on the data $d_\theta(t)$ is carried out by applying the maximum likelihood method; the likelihood function can be approximated by a multivariate gaussian distribution:

$$\mathcal{L}(d_\theta|\theta) = \mathcal{N} \exp\left\{-\frac{1}{2}\Delta\theta^i (C^{-1})^j_i \Delta\theta_j\right\} \tag{24}$$

where $\Delta\theta = \theta - \overline{\theta}$ and C is the covariance matrix; $C^{-1} \equiv \mathcal{F}$ is the Fisher matrix, and can be obtained as:

$$\mathcal{F}_{ij} = (\partial_i h|\partial_j h)\Big|_{\theta=\overline{\theta}} = 4\Re \int_0^\infty \frac{1}{S_n(f)} \frac{\partial h}{\partial\theta_i} \frac{\partial h^*}{\partial\theta_j}\Big|_{\theta=\overline{\theta}} df \tag{25}$$

in the frequency domain, where $S_n(f)$ is the characteristic noise spectral density of the detector, assumed to be known. The dyadic product $(a|b)$ is defined as

$$(a|b) \equiv 4\Re \int_0^\infty \frac{a(f)b^*(f)}{S_n(f)} df \tag{26}$$

This product allows to compare different frequency functions (as the waveforms), weighting the integration with the spectral noise.

Note that this approach is valid only in the gaussian approximation of the likelihood, and it could fail if the approximation is not satisfied: this usually happens at very low SNR value. The Signal to Noise ratio (SNR) is defined as

$$\frac{S}{N} \equiv \frac{(d|h)}{\sqrt{(h|h)}} = \sqrt{4\int_0^\infty \frac{h(f)h^*(f)}{S_n(f)} df} = \sqrt{(h|h)} \tag{27}$$

in the approximation of gaussian noise with null expectancy value; it gives a measure of the detectability of the signal: for low SNR threshold the False Alarm Rate (FAR) increases, namely the rate at which a false signal is detected as a real one. Thus it is necessary to set a SNR threshold that discards the events with lower SNR. This will obviously reject some real events with faint signal, so the trade-off between rejecting false events and so reducing the observable objects or accept an higher FAR to include faint sources will be a crucial aspect of the data analysis during the observational period. A common choice is taking the SNR threshold between 7 and 9.

The waveform h that is used as a model can be chosen from a set of analytical approximants from LALSimulation (part of LALSuite, see LIGO Scientific Collaboration et al. (2018)), a software package currently used by the LIGO/VIRGO/KAGRA collaboration for the analysis of GW data. The dependencies from LALSimulation are already implemented in GWFish.

The simulation capabilities of GWFish that are used in this analysis are:

- Parameter estimation (PE): the code can simulate the predicted parameters and errors, given a synthetic population of GW sources represented by suitable approximants.
- SNR for every synthetic object.

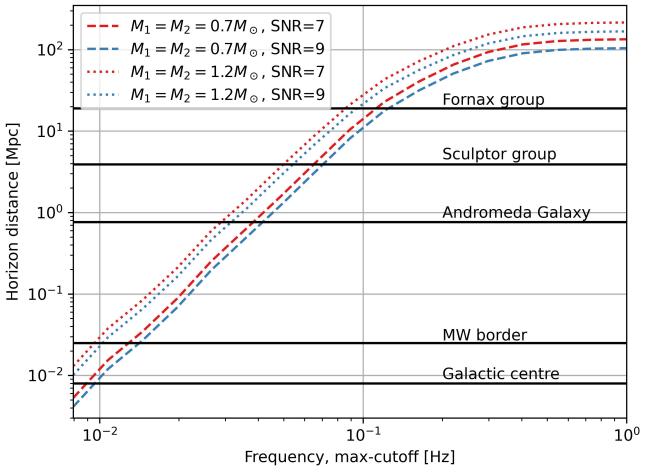

Figure 12. Horizons for a 0.7-0.7 $M_\odot$ and a 1.2-1.2 $M_\odot$ DWD, with SNR=7 or SNR=9. Some important position are shown as comparative scale.

• Horizon computation of a certain event with a chosen SNR, namely the maximum distance with optimal extrinsic parameters (such as the inclination) at which the event is still detectable.

A first application for the study of DWD population is the estimation of the horizon with respect to the frequency cutoff: as seen in sec. 5, at the end of LGWA observational period nearly all the observable DWDs would not have merged, but they would have reached a maximum GW frequency. Similarly, another frequency cutoff is imposed by the maximum merging frequency of the system, if the merging occurs during the observational period. This effect is implemented in GWFish by setting a `max_cutoff_frequency` parameter that cuts off all the frequencies above. This is a major effect in the determination of the event's SNR: a low cutoff implies a smaller horizon. This is visible in fig. 12, where some observable objects' distances are also shown. Comparing this plot with the merging frequencies found in sec. 2.3 (fig. 4) it is evident that since the merging frequency lies between ≈ 0.06 Hz for a 0.7 - 0.7$M_\odot$ DWD and ≈ 0.2 Hz for a 1.2 - 1.2$M_\odot$ DWD (the objects shown in the graph as approximate mass extremants for the formation of a SN Ia), it is conceivable that LGWA will correctly characterize the majority of the MW super-Chandrasekhar short-period ($f_{\rm GW} \leq 0.01$ Hz) DWD population, which is expected to be really thin, 43 ± 11 objects following the estimations in sec. 5.1. The sub-Chandrasekhar population is expected to present a even lower merging frequency, which combined with a minor power emission results in a difficult detectability. However the nearest population could anyway produce an observable (but faint) signal.

Regarding the extragalactic populations, fig. 12 shows that only very short period and very massive DWDs can be detected, up to ≈ 30 Mpc for the most massive systems of NeO-CO or NeO-NeO DWDs, and the expected frequency is such that a merging is expected in a short timescale.

6.0.1 Limitations of GWFish capabilities

At present, the GWFish code can provide excellent simulations of the detector's response only when the source is relatively close to the merging, but cannot simulate a nearly stationary low-mass source far from the merge. This allows to accurately simulate the detection of high-SNR events such as BH-BH, BH-NS, NS-NS events, whereas the nearly monochromatic DWDs (with frequency cutoff $\lesssim 50$ mHz, determined by the frequency reached at the end of the mission lifetime and not by the actual merging frequency) are more difficult to simulate. This does not imply that LGWA cannot detect these systems, which can become visible after 10 years of signal integration thanks to the fact that the GW emission is nearly monochromatic. However, this limit pose a strong constraint on the analysis of the synthetic population that has been generated in sec. 5: in fact, only a few of the galactic DWDs are suitable for the GWFish analysis, and only $\approx 1\%$ of the extragalactic population, despite already being an high-SNR population by construction.

For this reason, in the following is presented an analysis of the LGWA sensitivity referred only to the merging events. As seen in fig. 8, the generated population can sustain a constant SN Ia rate for ≈ 2 Myr; all the systems that merge within 1 Myr are selected, and for each the maximum frequency cutoff is calculated accordingly with the mass-radius relation presented in sec. 2.3. In particular, the cutoff is chosen as the frequency reached by the system when the distance between the DWDs becomes $2.5R_{\rm max}$, with $R_{\rm max}$ corresponding to the radius of the lighter WD in the binary system.

This analysis is to be intended as statistical: during the observational period the probability of observing a galactic SN Ia is negligible, while the expected SN Ia rate for extragalactic population is such that some merging events are expected within the mission lifetime. However, the super-Chandrasekhar DWDs are only a sub-population of the entire set of (potentially) observable DWDs which can merge during the observational period; in addition, the rate estimations could be biased by the relatively small number of observations. This statistical analysis is than a mean of probing the entire possible population that could be observed, with the relative abundaces (and thus probabilities) in the parameters space, imposed by the physical models used to generate the simulated population. The absolute abundance within the 10 years observational period can be derived simply by normalizing the 1 Myr period considered in the analysis.

Two different sub-populations are analyzed separately: in sec. 6.1 the super-Chandrasekhar DWDs in the MW are treated, as possible progenitors of SN Ia; the sub-Chandrasekhar population can not be analyzed due to the current version of GWFish. In sec. 6.2 is provided an estimation of the super-Chandrasekhar extragalactic population's detectability with distances up to 30 Mpc. Note that these analysis on the synthetic population should be completed with a proper complete analysis once the GWFish issues will be fixed: they are only a demonstration of the whole analysis pipeline that can be applied to the generated sample.

6.1 Super-Chandrasekhar MW population

Not all the simulated super-Chandrasekhar systems are detectable: a consistent part ($\approx 30\%$) is not treatable by GWFish, which introduces a significant systematic error in the final estimations. The

lacking population corresponds to the low-mass fraction of the super-Chandrasekhar population, which has a lower maximum frequency cutoff due to the larger radius following the mass-radius relation. This low cutoff is not treatable by the code; for the same reason, the entire sub-Chandrasekhar population is not yet analyzable. The rest of the systems are analyzed without any constrain on the SNR, that can be applied afterwards. The DWDs that can be simulated present a SNR$> 10^3$, with a typical SNR$\approx 2 \cdot 10^3$ and some well above $2 \cdot 10^4$.

In fig. 13 is shown the distribution of the SNR within the three populations. It is evident that the majority of the population comes from the thin disk, a consistent part from the bulge, and the thick disk is negligible.

The first row of fig. 14 shows the relation between the relative error of the luminosity distance and the SNR: it is clearly visible a neat linear border of the population in the logarithmic plane. For any GW, the expected d_L dependency will follow an inverse d_L^{-1} relation, so it is expected that $\partial_{d_L} h = -\frac{1}{d_L} h$. It follows that

$$\mathcal{F}_{d_L d_L} = (\partial_{d_L} h | \partial_{d_L} h) = \frac{(h|h)}{d_L^2} = \frac{\mathrm{SNR}^2}{d_L^2} \tag{28}$$

At the same time, the error on d_L is $\sigma_{d_L} = \sqrt{C_{d_L d_L}}$; the covariance matrix is obtained inverting the entire Fisher matrix $\mathcal{F}$, but for the estimation of σ_{d_L} only the entries of $\mathcal{F}$ that in C show a covariance with d_L are needed. In particular, the distance is strongly degenerated with the inclination angle θ, so that the covariance $\mathrm{cov}_{d_L \theta}$ can not be neglected. Inverting only the needed block results in the reduced Fisher matrix:

$$\tilde{\mathcal{F}} = \begin{bmatrix} \mathcal{F}_{d_L d_L} & \mathcal{F}_{d_L \theta} \\ \mathcal{F}_{\theta d_L} & \mathcal{F}_{\theta\theta} \end{bmatrix} = \begin{bmatrix} \sigma^2_{d_L} & \mathrm{cov}(\theta, d_L) \\ \mathrm{cov}(\theta, d_L) & \sigma^2_{\theta} \end{bmatrix}^{-1} \tag{29}$$

which leads to

$$\mathcal{F}_{d_L d_L} = \frac{1}{\sigma^2_{d_L}} \frac{1}{1 - \dfrac{\mathrm{cov}(\theta, d_L)^2}{\sigma^2_{d_L} \sigma^2_{\theta}}} = \frac{1}{\sigma^2_{d_L}} \cdot k \tag{30}$$

where the corrective factor to the simple $\frac{1}{\sigma^2_{d_L}}$ relation that would occur if all the covariances were 0 has been condensed in the factor $k = (1 - \rho^2)^{-1}$, where ρ is the Pearson correlation coefficient. Note that $k \geq 1$ since $-1 < \rho < 1$.

Matching eq. 30 and eq. 28 results in

$$\frac{\sigma_{d_L}}{d_L} = \frac{\sqrt{k}}{\mathrm{SNR}} \tag{31}$$

This means that with logarithmic axes the population will be characterized by the strong constrain of the diagonal $\log(\mathrm{SNR}) = \log(\sigma_{d_L}/d_L)$ corresponding to null covariance, but will extend over the diagonal for higher values of covariance. The degeneracy between d_L and θ can be very accentuated, so the population is expected to easily detach from the limit condition $k = 0$.

This is exactly what can be seen in the first row of fig. 14 with great precision.

A similar effect occurs in the second row of fig. 14, but in this case the correlation is between ra and dec, whose errors are used to calculate the 90% sky localization area, and the effect is less pronounced. It is worth noting that the sky localization precision that is reached spans from $\approx$ 1 arcsec (as) to $\approx$ 5 milliarcsec (mas); for comparison, the terrestrial optical observatories in the visible range can reach a seeing of $\approx$ 0.5 as, the space telescopes (for example, JWST) $\approx$ 0.1 as. With interferometric techniques even higher resolutions can be accomplished, as 2 mas for VLT or 5 mas for the ELT (under construction). These orders of magnitude make the LGWA resolution competitive in the next generation of astrophysical detectors within the framework of high-SNR merging events.

Finally, the third row shows the relation between σ_{d_L}/d_L and the 90% sky area, namely the two parameters that characterize the 3-dimensional localization capabilities of the detector. The SNR is still present as coloration of the objects. Note that the three perspectives presented in fig. 14 are the projections of the populations from the σ_{d_L}/d_L - sky area - SNR space.

Given the errors on sky localization and luminosity distance, it is possible to estimate the volume that contains the source as the portion of space identified by the 1σ errors on the localization parameters. This is a fundamental parameter, since to exactly locate a source (and possibly link the gravitational detection with optical observations) it should be contained in a reasonably small volume. The typical distances between stars in the MW strongly depends on the position, but an order of magnitude of the typical distances is around 0.1 - 10 pc. This means that the volume needed to identify a single star should be less than $\approx 10^{-3}$ pc^3, although for the population near the Solar System, more accessible to optical observations, higher volumes can be enough. In addition, optical characterization of the possible sources (e.g. via spectral classification) can further increase the minimum volume if needed. In fig. 15 is presented the relation between the distance and the volume: only a small part of the MW population lies under the (very strong) limit of 10^{-3} pc^3, however all the systems are limited in a maximum volume of less than 10^3 pc^3, which is enough to apply other identification techniques to better constrain the position of the source if it is visible to electromagnetic detectors.

Note that the exact positions of the single DWDs are not of great importance if the goal is to obtain a statistical characterization of the MW DWD population and match it with the observed SN Ia rate, as described in sec.2. On the contrary, it is crucial if the objective is to study the single system's properties to characterize a SN Ia progenitor.

In conclusion, for what concerns the super-Chandrasekhar population of the MW, LGWA offers a good characterization of the population, with errors that allow for an effective localization of the sources. The main source of error in this analysis comes from the simulation of the detector response by GWFish, which cannot simulate all the objects in the synthetic population, other than the errors that affect the population itself, already described in sec. 5.6.1.

6.2 Extragalactic population

Also for the extragalactic population an high percentage of the systems that merge can't be elaborated by the code; this fraction amounts at $\approx$ 37% of the total population. Given the estimation of the SN Ia rate obtained in sec. 6.2 associated with a local rate density of 3.67 SN Mpc^{-3} y^{-1}, it is expected to observe 1 or 2 SN events in a 10 Mpc radius during the 10 years observational period. This estimation however, despite being in accordance with the rates presented in Li

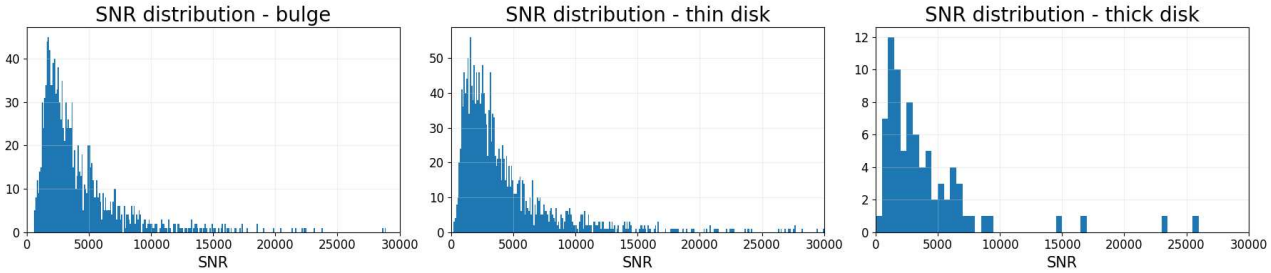

Figure 13. histograms of the SNR within the simulated MW population. Note the different vertical scales. For the thin disk population, the tail of the distribution continues above SNR=$3 \cdot 10^4$, but for graphical clarity the axis has been truncated.

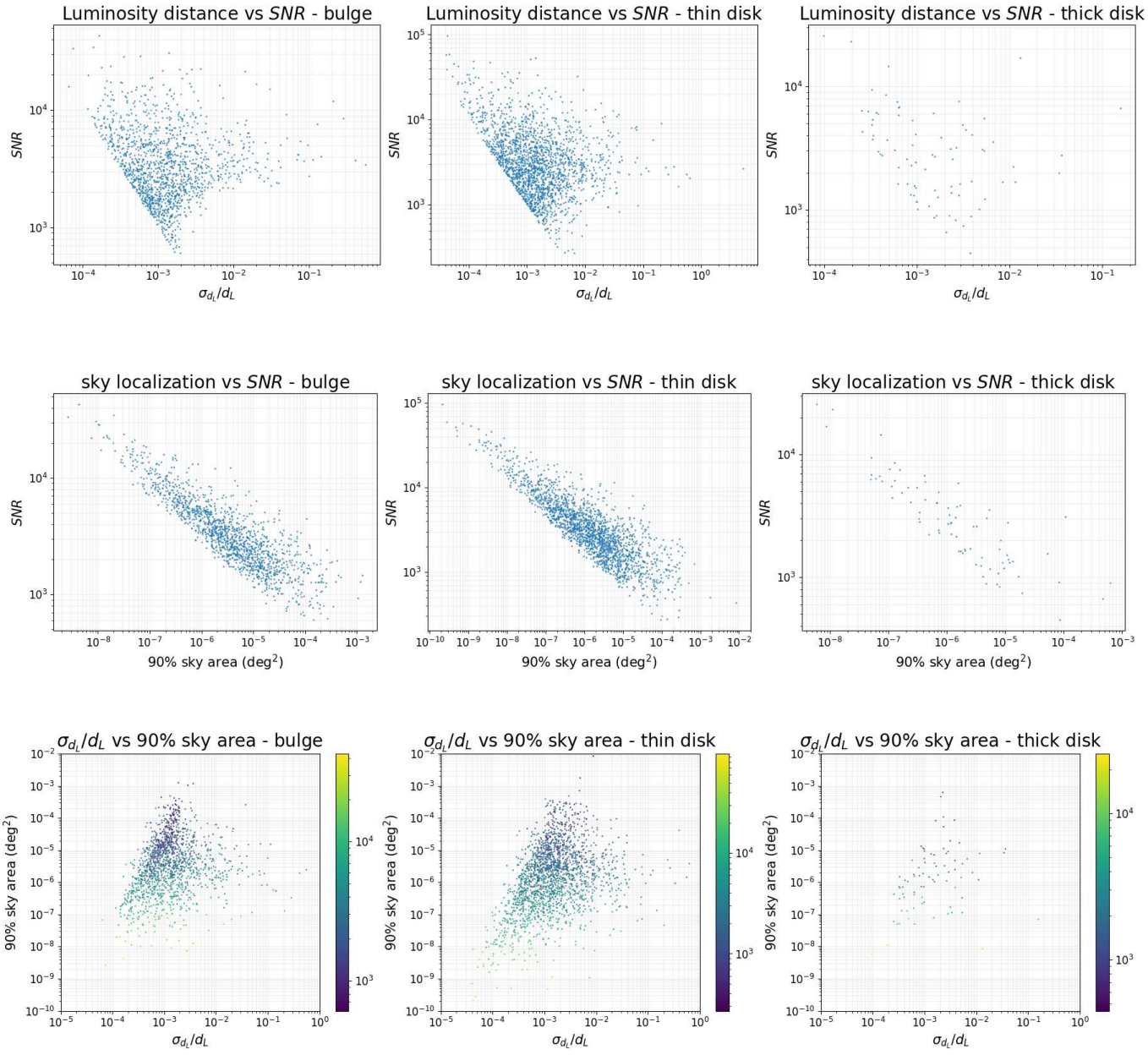

Figure 14. Up: MW population scatter plot with relative error on d_L (σ_{d_L}/d_L) vs SNR. Middle: scatter plot with relative error on d_L vs SNR. Down: scatter plot showing the relation between the relative error on d_L and sky localization (90% sky area in deg^2), with SNR colorbar.

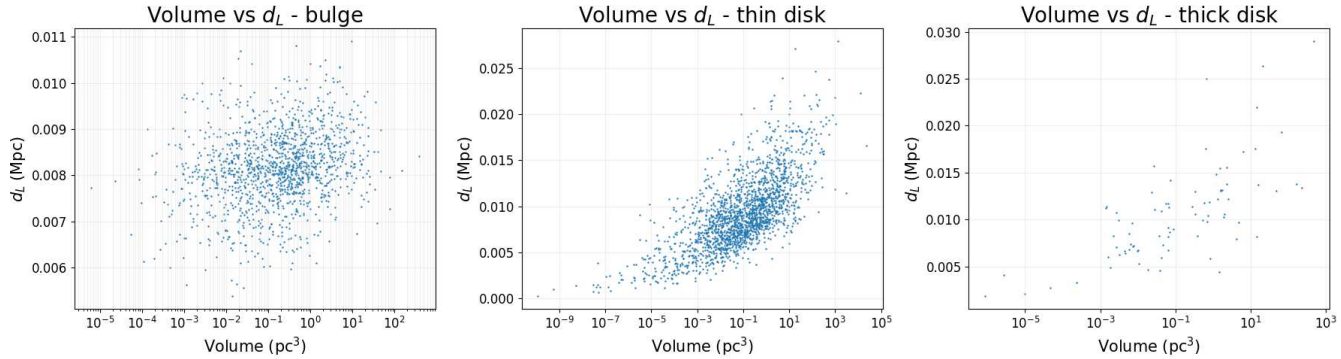

Figure 15. Distance - volume relation for the three super-Chandrasekhar MW populations.

et al. (2011), could be underestimated; as pointed out by Maoz & Mannucci (2012), the rate-size relation could be biased, and the parameters that have been used present anyway considerable errors. The observations with Zwicky Transient Facility (ZTF) hint at a much higher rate (Ajith et al. 2024), although the correction to account for unclassified SN introduces an large uncertainty in the total rate. For this analysis I used the rate previously derived to better account for the spatial distribution of the sources and for its accordance with the estimations of Li et al. (2011), however there is the possibility that the correct results should be obtained from a normalization of the used rate, namely by multiplying the final results by a fixed constant. In addition, note that the DWD population is obtained by the MW parameters distribution, thus a further bias is introduced in the extragalactic population, that could present different characteristics compared to the MW, for example in the mass distribution, although reproducing the same SN Ia rate. This bias is very difficult to correct, since a different SFH and initial parameter distribution should be considered for every galaxy, or at least for every morphological type.

The SNR distribution is presented in fig. 16. Differently from the MW analysis, there is an accumulation of events towards SNR=0, which corresponds to the furthest population, that is treatable by GWFish but not detectable by LGWA due to the distance. Two possible SNR thresholds (SNR=7 and SNR=9) are shown in the graph: it is clear that the choice of the SNR will heavily influence the number of such systems detected outside the MW, unlike for the MW merging population, where the detection is assured if a merging occurs (at least for a system with characteristics represented in the the analyzed sample). From the histogram plot, the population's SNR seems to be be well represented with a power-law distribution; in the plot is reported the power law

$$\frac{dN}{du} = n_0 \cdot u^{-\Sigma}$$

where the variable u represents the SNR (SNR units), and the exponent Σ is found to be $\Sigma \approx 3.4$. The normalization $n_0 \approx 2.3 \cdot 10^5$ is reported for completeness, although it does not play a physical role.

A better representation of the detection capabilities of LGWA for the extragalactic population is reported in fig. 17. In this plot is reported the 1σ volume in which the merging is identified, calculated as described in the previous section, and the luminosity distance of the system, namely of the host galaxy. It is very important to estimate whether the sources can be unambiguously linked to the host galaxies: as explained in sec. 2, if such identification is possible, an independent measurement of the luminosity distance can be performed, an so an independent calibration of the redshift-distance relation. To estimate a maximum volume $V_{\max}$ that can be tolerated (confusion limit), the HyperLeda catalogue is once again used: since the MW is located in a mass overdensity, the confusion limit is estimated in three different shells: from $D_l = 0$ Mpc to 10 Mpc, from 10 Mpc to 20 Mpc and finally from 20 Mpc to 30 Mpc. The average confusion limit is obtained as n^{-1}, where $n = N/V$ is the numerical density of the HyperLeda galaxies in the corresponding spatial shell. The resulting confusion limits are:

$$\begin{aligned} D_l \in (0, 10)\ \text{Mpc} &\quad \Rightarrow \quad V_{\max} = 10\ \text{Mpc}^3 \\ D_l \in (10, 20)\ \text{Mpc} &\quad \Rightarrow \quad V_{\max} = 15.5\ \text{Mpc}^3 \\ D_l \in (20, 30)\ \text{Mpc} &\quad \Rightarrow \quad V_{\max} = 29.8\ \text{Mpc}^3 \end{aligned}$$

These limits are reported in fig. 17. For the 10 Mpc shell, almost all the sources are included in the safe zone under the confusion limit. For the 20 Mpc shell, the majority of the population is below the limit, but a considerable fraction goes beyond $V_{\max}$, and the over-limit population is the majority for the 30 Mpc shell. Given the trend in the first 30 Mpc, it is conceivable that a particularly favourable event could be detected up to 40-45 Mpc; the rare occurrence of such events is partially compensated by the larger volume reached. Those events would be particularly important, not for the study of the SN Ia rates but for the distance calibration.

From the SNR coloration it is important to note that all the population that lies over the confusion limit has a SNR that is too low to allow a detection: with small variations depending on the chosen minimum SNR, the detection threshold roughly corresponds with the confusion limit (more likely, the SNR constraint is more selective than the confusion limit). This implies that if a merging of a super-Chandrasekhar DWD is detected, almost certainly the host galaxy is recognizable only by means of the LGWA GW observation. This would of course be important for an eventual SN Ia event following the merging, which could be observed by other detectors; prior to the merging, the LGWA detection would provide an estimation of the sky localization and the merging time of the system, that will allow preparing in advance the observation of the transient. After the merging, if an electromagnetic counterpart is detected it would provide additional data to better constrain the system parameters in the

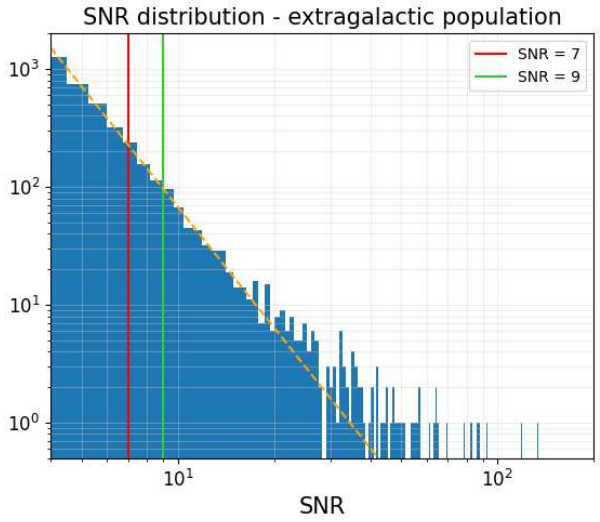

Figure 16. Histogram of the SNR of the extragalactic population. The limits SNR=7 and SNR=9 are shown as possible threshold for a detection. The dashed line is the power-law distribution that empirically matches the SNR distribution. Note that both the axes are logarithmic.

GW data analysis. If the counterpart is not detected, the localization capabilities of LGWA are much more important as they would be the only means of knowing the origin of the signal; this can occur if:

- The SN Ia event happens, but is obscured by the MW disk or by the host galaxy disk: this is an experimental problem that could eventually be resolved (for example, by means of a neutrino detection, see Wright et al. (2016), or a radio afterglow).
- The SN Ia event do not happen immediately after the merging: this would pose strong constraints on the current theoretical models.

In any case, the localization of the source is of primary importance; this analysis shows that for merging DWDs the confusion limit is not surpassed, due to the inevitable SNR threshold that limits the detection. Thus LGWA can fulfill the requirements needed to perform this type of research, under the more general conditions of detection.

7 CONCLUSIONS

The LGWA detector will give access to a whole new frequency band in the gravitational wave spectrum, spanning in the interval $(10^{-3}, 4)$ Hz, which is expected to contain a multitude of observable objects and new physics (see sec. 4). In particular, this work is focused on the study of double white dwarfs, which are expected to merge in the LGWA band, and are possible candidates for SN Ia progenitors, as discussed in sec. 2. A fiducial synthetic population of DWDs has been generated, following the latest and most reliable physical models regarding stellar structure, star formation, stellar evolution and mass distribution within the Milky Way and for the extragalactic population, calibrating the populations' sizes with the expected SN Ia rates. The construction of the synthetic population is thoroughly described in sec. 5. Afterwards, an analysis of the detectability of such objects is performed (sec. 6), using the Fisher-matrix technique through the code GWFish. Due to the current version of the code, only merging systems are analyzed; the main interest is to characterize the localization capabilities (SNR, error on the luminosity distance and sky localization) of LGWA with respect to the DWD population. For merging DWDs, LGWA can effectively identify the source as a single system in the MW and as a single galaxy for the extragalactic population. The precision that should be reached by the detector is enough to locate the object unambiguously and link it to a potential electromagnetic observation. The confusion limit however can be reached by some objects, especially for the extragalactic population, meaning that the safe margin is not wide, and the actual measurements will be challenging to perform. This implies that other studies are advisable on this topic, that should cover at least two aspects:

- A more detailed estimation of the properties of the expected sources, in particular for what regards the exact merging frequency of the DWDs, which introduces a frequency cutoff that is crucial to determine the SNR and the localization precision. A small variation of the frequency cutoff implies a considerable change in the SNR and localization quality. This estimation, being strictly determined by the physical interaction between the two WDs, is related to the second aspect:
- A precise modelization of the waveform, which is heavily affected by mass effects and does not follow the ideal waveform of two massive points (see sec. 3), especially in the latter phases of the merging. This aspect will be particularly important during the analysis of the actual data stream, which is currently performed with match filters but is expected to be far more difficult for the low frequency detectors such as LGWA. A better analysis pipeline could allow to lower the SNR threshold, making more sources detectable. On the other hand, the non-idealities will provide a lot of information regarding the physics that is involved in the merging process.

In this work, the monochromatic part of the synthetic population, namely the DWDs that do not merge during the mission lifetime, is not treated. The accurate analysis of spiraling DWDs will be matter for a future study, since this population represents the majority of the objects that could be visible in the Milky Way. The estimation of the SNR and potential localization of these sources is not trivial, since the power emission through GW is very weak, but the monochromatic signal can be integrated over the entire observing period of 10 years. Having already generated the synthetic population, this analysis will consist only in a proper estimation of the SNR and localization of the sources, similarly to what is shown in sec. 6 of this work. A possible simplified analytical approach to the SNR estimation is presented in Appendix A.

Acknowledgements

I wish to warmly thank the co-supervisor, Prof. Jan Harms, and the supervisor, Prof. Jean Pierre Zendri, for the professionalism and the support during the writing of this thesis. I am grateful to Dr. Enrico Cappellaro and Prof. Marica Branchesi for the helpful discussions on the SN Ia rates, and to Dr. Roberto Rampazzo for the conversations about galactic structure.

We acknowledge the usage of the HyperLeda database (http://leda.univ-lyon1.fr)

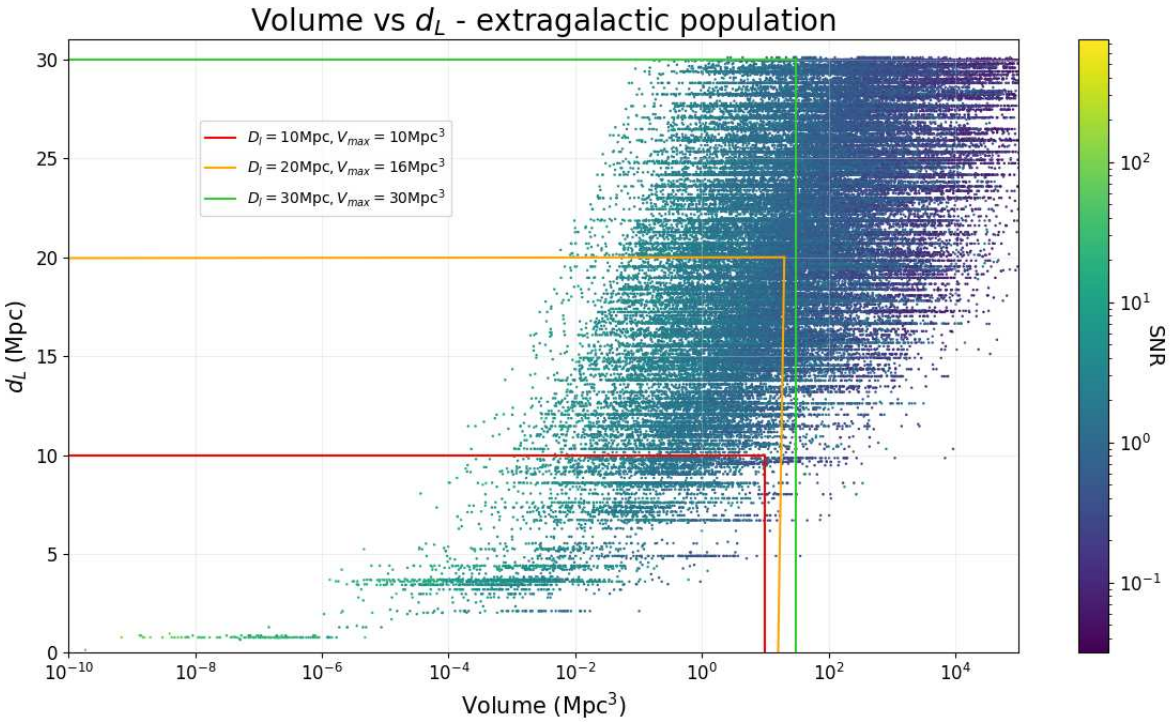

Figure 17. Scatter plot of the extragalactic merging population over 1 Myr. It is shown the relation between the luminosity distance D_l and the 1σ volume that contains the object. The SNR is present as coloration. In addition, the three coloured lines mark the maximum confusion limit required to identify the host galaxy (on average), described in sec. 6.2. The events are aligned on horizontal lines, as every line is relative to one galaxy, and the volume (and SNR) distribution varies over the line depending on the single source.

APPENDIX A

Analytical solution for stationary-source SNR

As seen in sec. 6, the usage of GWFish for stationary sources is not possible; in this appendix is provided a simplified estimation of the SNR for the synthetic populations at present, namely without considering only the merging phase, using an analytical approach. This analysis considers only some of the numerous parameters that were considered previously, and provides only the estimation of the SNR, and thus the detection/non-detection of the systems. In particular, the analysis accounts for:

- Luminosity distance, as the wave amplitude diminishes as D_l^{-1}.
- Mission duration: the integration of the signal during the mission lifetime has a direct impact on the SNR.
- GW frequency: the frequency associated with the system is considered as constant during the observational period, and is taken equal to the frequency cutoff that has been assigned to every system during the construction of the synthetic population.
- LGWA PSD: the sensitivity of the detector determines the SNR as shown in eq. 27.

The main sources of error are:

- Constant response tensor: the sky position of the source is not considered, so the waveform is mediated via a constant response tensor $\mathcal{R}$. As a result, the harmonic waveform can be directly expressed as a sinusoidal function.
- Not considering the inclination of the system: all the systems are considered as face-on, namely the best configuration. This will result in higher SNR.
- Stationary system approximation: for the majority of the systems this approximation is valid, however for the most high-frequency binaries the signal is not monochromatic and thus the approximation is not valid anymore. These systems are very few in the MW, while for the extragalactic population this error could be more important.
- Other parameters: while GWFish provides an accurate simulation of the waveform using all the parameters described in sec. 5, this modelization accounts only for a first-order two-mass inspiral. However, this effect is minor compared to the previous two.

For a stationary monochromatic source, the waveform is an harmonic oscillation

$$h_\Omega(t) = \mathcal{A}\cos(\Omega t) \tag{32}$$

with amplitude

$$\mathcal{A} = \mathcal{R}\frac{2(G\mathcal{M})^{5/3}(\pi f)^{2/3}}{c^4 D_l}$$

To obtain the frequency-domain waveform, a Fourier transform is applied:

$$h(\omega) = \int_0^T h_\Omega(t) e^{-i\omega t}\, dt$$

$$= \frac{T}{2}\mathcal{A}\left[\exp\left\{ iT\frac{\Omega-\omega}{2}\right\} S_-(\omega) + \exp\left\{ -iT\frac{\Omega+\omega}{2}\right\} S_+(\omega)\right] \quad (33)$$

where the two functions $S_\pm$ are defined as

$$S_\pm(\omega) = \frac{\sin\left(T\frac{\Omega\pm\omega}{2}\right)}{T\frac{\Omega\pm\omega}{2}} \quad (34)$$

The SNR can be analytically obtained with eq. 27; first one can show that the $h(\omega)h^*(\omega)$ part can be reduced to a Dirac's delta in the approximation of long observational period:

$$h(\omega)h^*(\omega) = \left(\frac{T\mathcal{A}}{2}\right)^2 \left[S_-^2 + S_+^2 + 2S_-S_+\cos(T\Omega)\right] \quad (35)$$

For $T >> 1$ this can be approximated with

$$h(\omega)h^*(\omega) \approx \left(\frac{T\mathcal{A}}{2}\right)^2 S_-^2 \approx \frac{2\pi T\mathcal{A}^2}{4}\delta(\omega) \quad (36)$$

considering that

$$\int_{-\infty}^{\infty} \frac{\sin^2(x)}{x^2}dx = \pi \quad (37)$$

with the variable change $x = T\frac{\Omega-\omega}{2}$. Rewriting the δ with $f = \frac{\omega}{2\pi}$ results in:

$$h(\omega)h^*(\omega) \approx \frac{T\mathcal{A}^2}{4}\delta(f) \quad (38)$$

and so

$$\mathrm{SNR} = \sqrt{4\int_0^\infty \frac{h(f)h^*(f)}{S_n(f)}df} = \sqrt{\frac{T\mathcal{A}^2}{S_n(f_{\mathrm{GW}})}} \quad (39)$$

Where f_{GW} is the frequency of the monochromatic source, namely the maximum frequency cutoff calculated for every object in the synthetic population.

As the average response tensor $\mathcal{R}$ is not known with precision, the expression is left as implicit, and it is not applied to the synthetic population. In future studies, the average tensor could be calculated (or simulated) in order to apply this formalism to stationary sources. Note that the explicit expression of $\mathcal{R}$ could include not only the frequency, but also a dependence from the sky position of the source and polarization of the GW, partially solving the approximations listed above.

REFERENCES

Abbott B. P., et al., 2017, Phys. Rev. Lett., 119, 161101
Ajith P., et al., 2024, arXiv e-prints, p. arXiv:2404.09181
Badenes C., Maoz D., 2012, The Astrophysical Journal Letters, 749, L11
Bi X., Harms J., 2024, arXiv e-prints, p. arXiv:2403.05118
Cignoni M., Degl'Innocenti S., Prada Moroni P. G., Shore S. N., 2006, A&A, 459, 783
Del Pozzo W., 2014, in Journal of Physics Conference Series. IOP, p. 012030, doi:10.1088/1742-6596/484/1/012030
Di Matteo P., 2016, Publ. Astron. Soc. Australia, 33, e027
Dupletsa U., et al., 2023, Astronomy and Computing, 42, 100671
Fantin N. J., et al., 2019, ApJ, 887, 148
Ferreras I., Wyse R. F. G., Silk J., 2003, MNRAS, 345, 1381
Haywood M., Di Matteo P., Snaith O., Calamida A., 2016, A&A, 593, A82
Helmi A., Babusiaux C., Koppelman H. H., Massari D., Veljanoski J., Brown A. G. A., 2018, Nature, 563, 85
Iben Icko J., Laughlin G., 1989, ApJ, 341, 312
Jackim R., Heyl J., Richer H., 2024, arXiv e-prints, p. arXiv:2404.07388
Korol V., Rossi E. M., Groot P. J., Nelemans G., Toonen S., Brown A. G. A., 2017, MNRAS, 470, 1894
Korol V., et al., 2020, A&A, 638, A153
Kraan-Korteweg R. C., Lahav O., 2000, A&ARv, 10, 211
LIGO Scientific Collaboration Virgo Collaboration KAGRA Collaboration 2018, LVK Algorithm Library - LALSuite, Free software (GPL), doi:10.7935/GT1W-FZ16
Leonard D. C., 2007, The Astrophysical Journal, 670, 1275
Li W., Chornock R., Leaman J., Filippenko A. V., Poznanski D., Wang X., Ganeshalingam M., Mannucci F., 2011, Monthly Notices of the Royal Astronomical Society, 412, 1473
Lorén-Aguilar P., Guerrero J., Isern J., Lobo J. A., García-Berro E., 2005, Monthly Notices of the Royal Astronomical Society, 356, 627
Makarov D., Prugniel P., Terekhova N., Courtois H., Vauglin I., 2014, A&A, 570, A13
Maoz D., Mannucci F., 2012, Publications of the Astronomical Society of Australia, 29, 447–465
McMillan P. J., 2017, MNRAS, 465, 76
Mor R., Robin A. C., Figueras F., Antoja F., Roca-Fàbrega S., Luri X., 2019, in The Gaia Universe. p. 42, doi:10.5281/zenodo.3146470
Padmanabhan T., 2001, Cambridge University Press, Theoretical Astrophysics vol. II
Pascale M., et al., 2024, arXiv e-prints, p. arXiv:2403.18902
Peters P. C., Mathews J., 1963, Physical Review, 131, 435
Phillips M. M., 1993, ApJ, 413, L105
Portegies Zwart S. F., Verbunt F., 1996, A&A, 309, 179
Radice D., Dai L., 2019, European Physical Journal A, 55, 50
Riess A. G., Press W. H., Kirshner R. P., 1995, ApJ, 438, L17
Shen K. J., Bildsten L., Kasen D., Quataert E., 2012, The Astrophysical Journal, 748, 35
Snaith O., Haywood M., Di Matteo P., Lehnert M. D., Combes F., Katz D., Gómez A., 2015, A&A, 578, A87
Toonen S., Nelemans G., Portegies Zwart S., 2012, A&A, 546, A70
Valentino E. D., et al., 2021, Classical and Quantum Gravity, 38, 153001
Vergely J. L., Lançon A., Mouhcine 2002, A&A, 394, 807
Wang B., Han Z., 2012, New Astronomy Reviews, 56, 122
Webbink R. F., 1984, ApJ, 277, 355
Weber J., 1962, proceedings of "Les théories relativistes de la gravitation : actes du colloque international", pp 441–450
Weber J., 1967, Phys. Rev. Lett., 18, 498
Weber J., 1970, Phys. Rev. Lett., 24, 276
Wright W. P., Nagaraj G., Kneller J. P., Scholberg K., Seitenzahl I. R., 2016, Phys. Rev. D, 94, 025026
van Heijningen J. V., et al., 2023, Journal of Applied Physics, 133, 244501

This paper has been typeset from a TEX/LATEX file prepared by the author.